

**MEASUREMENT OF MULTIJET CROSS-SECTION RATIOS IN  
PROTON-PROTON COLLISIONS WITH THE CMS DETECTOR AT  
THE LHC**

A THESIS

Submitted to the  
FACULTY OF SCIENCE  
PANJAB UNIVERSITY, CHANDIGARH  
for the degree of

**DOCTOR OF PHILOSOPHY**

**2017**

**Anterpreet Kaur**

DEPARTMENT OF PHYSICS  
CENTRE OF ADVANCED STUDY IN PHYSICS  
PANJAB UNIVERSITY, CHANDIGARH  
INDIA



*Dedicated to*  
*my Grand-Parents*

*&*

*Parents*









# Contents

List of Figures	xī
-----------------	----

List of Tables	xvii
----------------	------

---

1 Measurement of the Differential Inclusive Multijet Cross Sections and their Ratio	1
1.1 Data Samples . . . . .	2
1.1.1 Monte Carlo Samples . . . . .	3
1.2 Event Selection . . . . .	4
1.2.1 Trigger Selection . . . . .	4
1.2.2 Primary Vertex Selection . . . . .	8
1.2.3 Missing Transverse Energy . . . . .	8
1.2.4 Jet Identification . . . . .	9
1.2.4.1 Jet ID Efficiency . . . . .	10
1.2.5 Jet Energy Corrections and Selection . . . . .	13
1.3 Comparison with Simulated Events . . . . .	14
1.3.1 Pile-up Reweighting . . . . .	14
1.3.2 Cross Section Comparison . . . . .	14
1.4 Jet Energy Resolution (JER) . . . . .	16



---

1.5	Unfolding . . . . .	21
1.5.1	Response matrices . . . . .	22
1.5.2	Closure test . . . . .	25
1.5.3	Unfolding measurement . . . . .	27
1.6	Experimental uncertainties . . . . .	28
1.6.1	Luminosity measurement uncertainty . . . . .	28
1.6.2	Statistical uncertainty . . . . .	28
1.6.3	Jet Energy Corrections uncertainties . . . . .	30
1.6.4	Unfolding uncertainty . . . . .	31
1.6.5	Total experimental uncertainty . . . . .	32
<b>Appendix A</b>		<b>35</b>
A.1	Individual sources of Jet Energy Correction uncertainties . . . . .	36
<b>Bibliography</b>		<b>39</b>
<b>Reprints</b>		<b>41</b>



# List of Figures

1.1	Trigger efficiencies turn-on curves for the single jet trigger paths used in the analysis. To determine the 99% efficiency threshold, the trigger turn-on curves are fitted using a sigmoid function (blue line), taking into account the uncertainties using Clopper-Pearson confidence intervals [1]. . . . .	7
1.2	Missing transverse energy fraction of the total transverse energy per event in data (black solid circles) and simulated Monte Carlo events (blue histogram) in inclusive 2-jet (left) and 3-jet events (right). To remove background and noise, events with a fraction exceeding a certain threshold, here indicated with the red dashed line, are rejected. .	9
1.3	The fractions of jet constituents as observed in data (black solid circles) and simulated Monte Carlo events (blue histogram) for different types of PF candidates for inclusive 2-jet events. Data and simulations are normalized to the same number of events. The distributions are shown after the application of the jet ID. . . . .	11
1.4	The fractions of jet constituents as observed in data (black solid circles) and simulated Monte Carlo events (blue histogram) for different types of PF candidates for inclusive 3-jet events. Data and simulations are normalized to the same number of events. The distributions are shown after the application of the jet ID. . . . .	12

- 
- 1.5 The jet ID efficiency studied using a tag-and-probe technique on dijet event topologies, is shown as a function of  $H_{T,2}/2$  for inclusive 2-jet (left) and 3-jet events (right) and it always exceeds 99%. . . . . 13
- 1.6 Number of reconstructed vertices in data (black solid circles) and simulated Monte Carlo events (blue histogram) before (left) and after (right) the pile-up reweighting. . . . . 15
- 1.7 The differential cross sections are compared for data (black solid circles) and LO MADGRAPH5 + PYTHIA6 (MG5+P6) Monte Carlo (red empty circles), at reconstructed level with NLO theory predictions (blue histogram), as a function  $H_{T,2}/2$  for inclusive 2-jet events (left) and 3-jet events (right). Ratios of data to the Monte Carlo predictions (red line) as well as to the NLO predictions (blue line) are shown in bottom panel of each plot. . . . . 15
- 1.8 Fitting of the resolution distribution as a function of  $H_{T,2}/2$  for inclusive 2-jet (left) and for inclusive 3-jet events (right). The blue line shows the double-sided Crystal Ball function fit of  $\frac{\text{Reco } H_{T,2}/2}{\text{Gen } H_{T,2}/2}$  in each Gen  $H_{T,2}/2$  bin, overlayed by Gaussian fitting the core of the resolution (red line). . . . . 18
- 1.9 Comparison of jet energy resolution calculated using Crystal-Ball fit function (blue solid circles) and Gaussian fit function (red solid circles) for inclusive 2-jet events (left) and for inclusive 3-jet events (right). 19
- 1.10 Jet energy resolution (JER) is shown as a function of Gen  $H_{T,2}/2$  for inclusive 2-jet events (left) and for inclusive 3-jet events (right). JER (black solid circles) is fitted by using the modified NSC-formula (blue solid line) which is extrapolated to 80 GeV and upto 2 TeV (red dashed line) to consider the migration into lower as well as higher bins. 19

- 1.11 MADGRAPH5 + PYTHIA6 Gen smeared using extracted jet energy resolution (JER) shows a discrepancy from simulated Reco as Smeared Gen/Gen ratio (red line) does not match with Reco/Gen ratio (blue line), for both inclusive 2-jet (left) and inclusive 3-jet events (right). Smeared Gen/Gen ratio (pink line) where Gen is smeared using 30% reduced JER matches with simulated Reco/Gen ratio (blue line) within the statistical fluctuations. Hence an additional unfolding uncertainty is attributed by comparison to 30% reduced JER. . . . . 21
- 1.12 Fitted CT10-NLO spectrum of differential cross section as a function of  $H_{T,2}/2$  (green solid circles) using Function I (top) defined in Eq. 1.9 and using Function II (bottom) given by Eq. 1.12, for inclusive 2-jet events (left) and for inclusive 3-jet events (right). To consider the migration to lower  $H_{T,2}/2$  bins, the fit functions described by red lines are extrapolated to 80 GeV (blue dashed lines). . . . . 24
- 1.13 The response matrices are derived using the Toy Monte Carlo and forward smearing method, for inclusive 2-jet (left) and inclusive 3-jet events (right). The matrices are normalized to the number of events in each column and are diagonal with small off-diagonal migrations between close-by  $H_{T,2}/2$  bins. . . . . 25
- 1.14 Closure test of the unfolding technique where the smeared spectrum obtained from Toy Monte Carlo method (Measured<sub>Toy</sub>), is unfolded using the constructed response matrices (obtained by forward smearing the randomly generated spectrum (Gen<sub>Toy</sub>) using extracted jet energy resolution (JER)). As expected, the unfolded Measured<sub>Toy</sub> spectrum matches exactly with Gen<sub>Toy</sub> spectrum as the ratio of these distributions is perfectly flat at one for both  $n_j \geq 2$  (left) and  $n_j \geq 3$  events (right). . . . . 26

- 1.15 Reco MADGRAPH5 + PYTHIA6 Monte Carlo (MG5+P6 MC) differential cross section distributions unfolded with the response matrices (obtained by forward smearing the randomly generated spectrum (Gen) using extracted jet energy resolution (JER)), does not give a good closure with Gen MG5+P6 MC (blue line), for inclusive 2-jet (left) and inclusive 3-jet events (right). After performing the unfolding using 30% reduced JER, a good closure is obtained (red line). . . . 26
- 1.16 The unfolded differential cross sections as a function of  $H_{T,2}/2$  are compared with that of the measured one for inclusive 2-jet (left) and inclusive 3-jet events (right). The unfolding is done with response matrices using JER (blue solid circles) as well as 30% reduced JER (red solid circles). The difference between both is taken as an additional uncertainty on the unfolded measurement. . . . . 27
- 1.17 The fractional statistical uncertainties of the measured (blue line) and the unfolded data (red line) for inclusive 2-jet events (left) and for inclusive 3-jet events (right). The statistical uncertainty increases slightly after unfolding. . . . . 29
- 1.18 Correlations of the statistical uncertainty introduced by the unfolding procedure for inclusive 2-jet events (left) and and 3-jet events (right). There is a significant correlation or anti-correlation between neighbouring bins through bin migrations. . . . . 29

1.19	Overview of all experimental uncertainties affecting the cross section measurement for inclusive 2-jet (left) and inclusive 3-jet (right). The error bars indicate the statistical uncertainty after unfolding. The colored lines give the uncertainties resulting of jet energy scale, luminosity, unfolding and residual effects. The total uncertainty is calculated by adding in quadrature the individual sources of uncertainty.	
	<b>JEC</b> <b>Unfolding</b> <b>Luminosity</b> <b>Residual</b> <b>uncorrelated</b> . . . . .	33
A.1	The relative size of the jet energy correction (JEC) uncertainties for individual sources are shown for inclusive 2-jet (top) and 3-jet events cross sections (middle) and cross section ratio $R_{32}$ (bottom). On left, JEC uncertainties are evaluated from <b>AbsoluteStat</b> , <b>AbsoluteScale</b> , <b>AbsoluteMPFBias</b> and <b>Fragmentation</b> sources whereas on right, these are evaluated from <b>SinglePionECAL</b> , <b>SinglePionHCAL</b> and <b>FlavorQCD</b> sources. . . . .	36
A.2	The relative size of the jet energy correction (JEC) uncertainties for individual sources are shown for inclusive 2-jet (top) and 3-jet events cross sections (middle) and cross section ratio $R_{32}$ (bottom). On left, JEC uncertainties are evaluated from <b>RelativeJEREC1</b> , <b>RelativeJEREC2</b> , <b>RelativePtBB</b> and <b>RelativeJERHF</b> sources whereas on right, these are evaluated from <b>RelativePtEC1</b> , <b>RelativePtEC2</b> , <b>RelativePFSR</b> and <b>RelativePtHF</b> sources. . . . .	37

A.3	The relative size of the jet energy correction (JEC) uncertainties for individual sources are shown for inclusive 2-jet (top) and 3-jet events cross sections (middle) and cross section ratio $R_{32}$ (bottom). On left, JEC uncertainties are evaluated from RelativeStatFSR, RelativeStatEC2 and RelativeStatHF sources whereas on right, these are evaluated from PileUpDataMC, PileUpPtRef, PileUpPtBB, PileUpPtEC1, PileUpPtEC2 and PileUpPtHF sources. . . . .	38
-----	--	----



# List of Tables

1.1	Four data sets collected in run periods A, B,C and D during 2012, along with the corresponding run numbers and luminosity. . . . .	3
1.2	The official Monte Carlo produced samples generated in phase space slices in $H_T$ with the generator MADGRAPH5 and interfaced to PYTHIA6 for the parton shower and hadronization of the events. The cross section and number of events generated are mentioned for each sample. . . . .	4
1.3	List of all single jet trigger paths used in the analysis. The column $H_{T,2}/2$ , 99% indicates the value of $H_{T,2}/2$ at which each trigger exhibits an efficiency larger than 99%. The last column reports the effective luminosity seen by each trigger. This number, divided by the total integrated luminosity of $19.71 \text{ fb}^{-1}$ , gives the effective prescale applied on a trigger over the whole run period. . . . .	5
1.4	The jet ID removes noise and fake jets based on the properties of the reconstructed jets and the clustered particle candidates. All the selection cuts which are recommended by the JETMET group are applied [2]. . . . .	10

1.5	JETMET working group at CMS has shown that the jet energy resolution in data is actually worse than in simulation [3]. The scaling factors need to be applied to the reconstructed jet transverse momentum in simulated events to match the resolution in data. The uncertainty on the resolution is given by an upwards and downwards variation $c_{up}$ and $c_{down}$ of the smearing factor $c_{central}$ . . . . .	17
1.6	The parameters obtained by fitting the relative resolution as a function of $H_{T,2}/2$ , using the modified NSC formula, for inclusive 2-jet and inclusive 3-jet events. . . . .	20
1.7	Overview of all experimental uncertainties affecting the cross section measurement. . . . .	32

# Chapter 1

## Measurement of the Differential Inclusive Multijet Cross Sections and their Ratio

The inclusive  $n$ -jet event samples include the events with number of jets  $\geq n$ , where  $n = 2$  and 3 in the current study. The inclusive multijet event yields are transformed into a differential cross section which is defined as :

$$\frac{d\sigma}{d(H_{T,2}/2)} = \frac{1}{\epsilon \mathcal{L}_{\text{int,eff}}} \frac{N_{\text{event}}}{\Delta(H_{T,2}/2)} \quad (1.1)$$

where  $N_{\text{event}}$  is the number of inclusive 2- or 3-jet events counted in an  $H_{T,2}/2$  bin,  $\epsilon$  is the product of the trigger and jet selection efficiencies, which are greater than 99%,  $\mathcal{L}_{\text{int,eff}}$  is the effective integrated luminosity, and  $\Delta(H_{T,2}/2)$  are the bin widths. The measurements are reported in units of (pb/GeV).

The differential inclusive multijet cross sections are measured as a function of the average transverse momentum,  $H_{T,2}/2 = \frac{1}{2}(p_{T,1} + p_{T,2})$ , where  $p_{T,1}$  and  $p_{T,2}$  denote the transverse momenta of the two leading jets. The cross section ratio  $R_{32}$ , defined in Eq. 1.2 is obtained by dividing the differential cross sections of inclusive

3-jet events to that of inclusive 2-jet one, for each bin in  $H_{T,2}/2$ .

$$R_{32} = \frac{\frac{d\sigma_{3-jet}}{d(H_{T,2}/2)}}{\frac{d\sigma_{2-jet}}{d(H_{T,2}/2)}} \quad (1.2)$$

For inclusive 2-jet events ( $n_j \geq 2$ ) sufficient data are available up to  $H_{T,2}/2 = 2 \text{ TeV}$ , while for inclusive 3-jet events ( $n_j \geq 3$ ) and the ratio  $R_{32}$ , the accessible range in  $H_{T,2}/2$  is limited to  $H_{T,2}/2 < 1.68 \text{ TeV}$ .

## 1.1 Data Samples

This measurement uses the data collected at the center of mass energy of 8 TeV by CMS experiment in the 2012 run period of the LHC. The 2012 data is taken in four periods A, B, C, D and the data sets are divided into samples according to the run period. Further each sample is grouped into subsets based on the trigger decision. For run B-D, the **JetMon** stream datasets contain prescaled low trigger threshold paths (HLTPFJet40, 80, 140, 200 and 260) while the **JetHT** stream datasets contain unprescaled high threshold trigger paths (HLT PFJet320 and 400). For run A, the **Jet** stream contains all the above mentioned trigger paths. The data to be used in physics analysis must satisfy a certain criteria which include proper performance of all detector subsystems as well as the passing of data quality monitoring (DQM) steps during the validation process. CMS uses JSON (Java Script Object Notation) format files to store the range of good lumi sections within a run. In the current analysis, the applied certification file<sup>1</sup> is based on the final event reconstruction of the 2012 CMS data sets. The datasets used in the current study are mentioned in the Table 1.1 along with the luminosity of each dataset.

---

<sup>1</sup>Cert\_190456-208686\_8TeV\_22Jan2013ReReco\_Collisions12.JSON

Table 1.1: Four data sets collected in run periods A, B,C and D during 2012, along with the corresponding run numbers and luminosity.

Run	Run range	Data set	Luminosity $\text{fb}^{-1}$
A	190456-193621	/Jet/Run2012A-22Jan2013-v1/AOD	0.88
B	193834-196531	/Jet[Mon,HT]/Run2012B-22Jan2013-v1/AOD	4.41
C	198022-203742	/Jet[Mon,HT]/Run2012C-22Jan2013-v1/AOD	7.06
D	203777-208686	/Jet[Mon,HT]/Run2012D-22Jan2013-v1/AOD	7.37

The data sets have the LHC luminosity increasing with period, full data sample of 2012 corresponds to an integrated luminosity of  $19.71 \text{ fb}^{-1}$ .

### 1.1.1 Monte Carlo Samples

To have a comparison of data results with the simulated events, the MADGRAPH5 [4] Monte-Carlo (MC) event generator has been used. The MADGRAPH5 generates matrix elements for High Energy Physics processes, such as decays and  $2 \rightarrow n$  scatterings. The underlying event is modeled using the tune Z2\*. It has been interfaced to PYTHIA6 [5] by the LHE event record [6], which generates the rest of the higher-order effects using the Parton Showering (PS) model. Matching algorithms ensure that no double-counting occurs between the tree-level and the PS-model-generated partons. The MC samples are processed through the complete CMS detector simulation to allow studies of the detector response and compare to measured data on detector level.

The cross section measured as a function of the transverse momentum  $p_T$  or the scalar sum of the transverse momentum of all jets  $H_T$  falls steeply with the increasing  $p_T$ . So in the reasonable time, it is not possible to generate a large number of high  $p_T$  events. Hence, the events are generated in the different phase-space region binned in  $H_T$  or the leading jet  $p_T$ . Later on, the different phase-space regions are added together in the data analyses by taking into account the cross section of the different phase-space regions. The official CMS MADGRAPH5

+ PYTHIA6 (MG5+P6) MC samples used in this analysis are generated as slices in the  $H_T$  phase-space are tabulated in Table 1.2 along with their cross sections and number of events generated.

Table 1.2: The official Monte Carlo produced samples generated in phase space slices in  $H_T$  with the generator MADGRAPH5 and interfaced to PYTHIA6 for the parton shower and hadronization of the events. The cross section and number of events generated are mentioned for each sample.

Generator	Sample	Events	Cross Section pb
MADGRAPH5 + PYTHIA 6	/QCD_HT-100To250_TuneZ2star_8TeV-madgraph-pythia6/ Summer12_DR53X-PU_S10_START53_V7A-v1/AODSIM	50129518	$1.036 \times 10^7$
	/QCD_HT-250To500_TuneZ2star_8TeV-madgraph-pythia6/ Summer12_DR53X-PU_S10_START53_V7A-v1/AODSIM	27062078	$2.760 \times 10^5$
	/QCD_HT-500To1000_TuneZ2star_8TeV-madgraph-pythia6/ Summer12_DR53X-PU_S10_START53_V7A-v1/AODSIM	30599292	$8.426 \times 10^3$
	/QCD_HT-1000ToInf_TuneZ2star_8TeV-madgraph-pythia6/ Summer12_DR53X-PU_S10_START53_V7A-v1/AODSIM	13843863	$2.040 \times 10^2$

## 1.2 Event Selection

To yield a multijet sample with high purity and high selection efficiency, the events are selected according to several quality criteria. This event selection also reduces beam induced background, detector-level noise and jets arising from fake calorimeter energy deposits.

### 1.2.1 Trigger Selection

CMS implements a trigger system organized in two levels, in order to reduce the amount of recorded events to a sustainable rate. This analysis deals with jets in the final state, so single jet trigger paths are used to select events in data which consists of one L1 trigger seed and multiple HLT filters. The L1 jet trigger uses transverse energy sums computed using both HCAL and ECAL in the central region ( $|\eta| < 3.0$ ) or HF in the forward region ( $|\eta| > 3.0$ ). A more elaborate but still very fast algorithm, the “jet finder”, is then implemented on the energy cluster but

with a finer segmentation in order to select the raw object for the HLT trigger : the algorithm makes use of a cone size in order to cluster in a primitive jet the calorimeter towers whose energy is larger than the seed threshold. If the primitive HLT jet has an energy above the threshold set by the trigger, the event is selected and the collection of recorded data is saved and stored in streams. The single jet triggers used for this analysis are tabulated in Table 1.3. HLT\_PFJetX implies that there is at-least one jet in the event, whose  $p_T > X$  (GeV). The L1 trigger has a lower threshold to ensure full efficiency versus  $p_T$  of the HLT trigger. The  $p_T$  spectrum is steeply falling and hence the rates for low- $p_T$  jets are very high. So it is not feasible to use a single unprescaled trigger for the selection of all required events. To collect sufficient data in the lower part of the  $p_T$  spectrum, different five prescaled low- $p_T$  trigger paths, each with different prescale value, are used. Also, one unprescaled trigger i.e. HLT\_Jet320 is used in the high  $p_T$  region, in which the rate is sufficiently small to collect and store all events. During the reconstruction of the spectrum, the prescales have been taken into the account.

Table 1.3: List of all single jet trigger paths used in the analysis. The column  $H_{T,2}/2$ , 99% indicates the value of  $H_{T,2}/2$  at which each trigger exhibits an efficiency larger than 99%. The last column reports the effective luminosity seen by each trigger. This number, divided by the total integrated luminosity of  $19.71 \text{ fb}^{-1}$ , gives the effective prescale applied on a trigger over the whole run period.

Trigger Path	L1 threshold GeV	HLT threshold GeV	$H_{T,2}/2$ , 99% GeV	Eff. Lumi $\text{fb}^{-1}$
HLT_PFJet80	36	80	120.0	$0.21 \times 10^{-2}$
HLT_PFJet140	68	140	187.5	$0.56 \times 10^{-1}$
HLT_PFJet200	92	200	262.5	0.26
HLT_PFJet260	128	260	345.0	1.06
HLT_PFJet320	128	320	405.0	19.71

The efficiency of each trigger, as a function of the measured observable, is described by the turn-on curves with a rising part, where the trigger is partly inefficient, until a plateau region, corresponding to the region of full efficiency of the trigger. Hence it is necessary to determine the threshold above which a trigger becomes fully efficient. It is defined as the value at which the efficiency exceeds

99%. In the assumption that the reference trigger HLT\_PFJetX is fully efficient in the considered region of the phase space, the trigger efficiency for HLT\_PFJetY is defined as Eq. 1.3. The value of X is chosen previous to that of Y in  $p_T$  ordering from the trigger list so that the higher trigger condition can be emulated from the lower trigger path.

$$\epsilon_{\text{HLT\_PFJetY}} = \frac{H_{T,2}/2 \left( \text{HLT\_PFJetX} + (\text{L1Object\_}p_T > Z) + (\text{HLTOBJECT\_}p_T > Y) \right)}{H_{T,2}/2(\text{HLT\_PFJetX})} \quad (1.3)$$

where Y indicates the  $p_T$  threshold of HLT\_PFJetY and Z is the L1 seed value corresponding to the trigger path HLT\_PFJetY. The denominator represents the number of events for which the reference trigger path HLT\_PFJetX has been fired. The numerator is the number of events for which HLT\_PFJetX has been fired along the  $p_T$  of L1Object  $\geq Z$  and the  $p_T$  of HLTOBJECT  $\geq Y$ . For example, in order to obtain turn-on curve for HLT\_PFJet260, the reference HLT path HLT\_PFJet200 is chosen, the  $p_T$  cut on L1Object is 128 GeV and  $p_T$  cut on HLTOBJECT is 260 GeV. The uncertainty on the efficiency is indicated by error bars which represent Clopper-Pearson confidence intervals [1]. To determine the point, at which the trigger efficiency is larger than 99%, the turn-on distribution is fitted using a sigmoid function described in Eq. 1.4. The trigger turn-on curves as a function of  $H_{T,2}/2$  can be seen in Fig. 1.1 which are described by a sigmoid function (blue line).

$$f_{fit}(x) = \frac{1}{2} \left( 1 + \text{erf} \left( \frac{x - \mu}{\sqrt{2}\sigma} \right) \right) \quad (1.4)$$



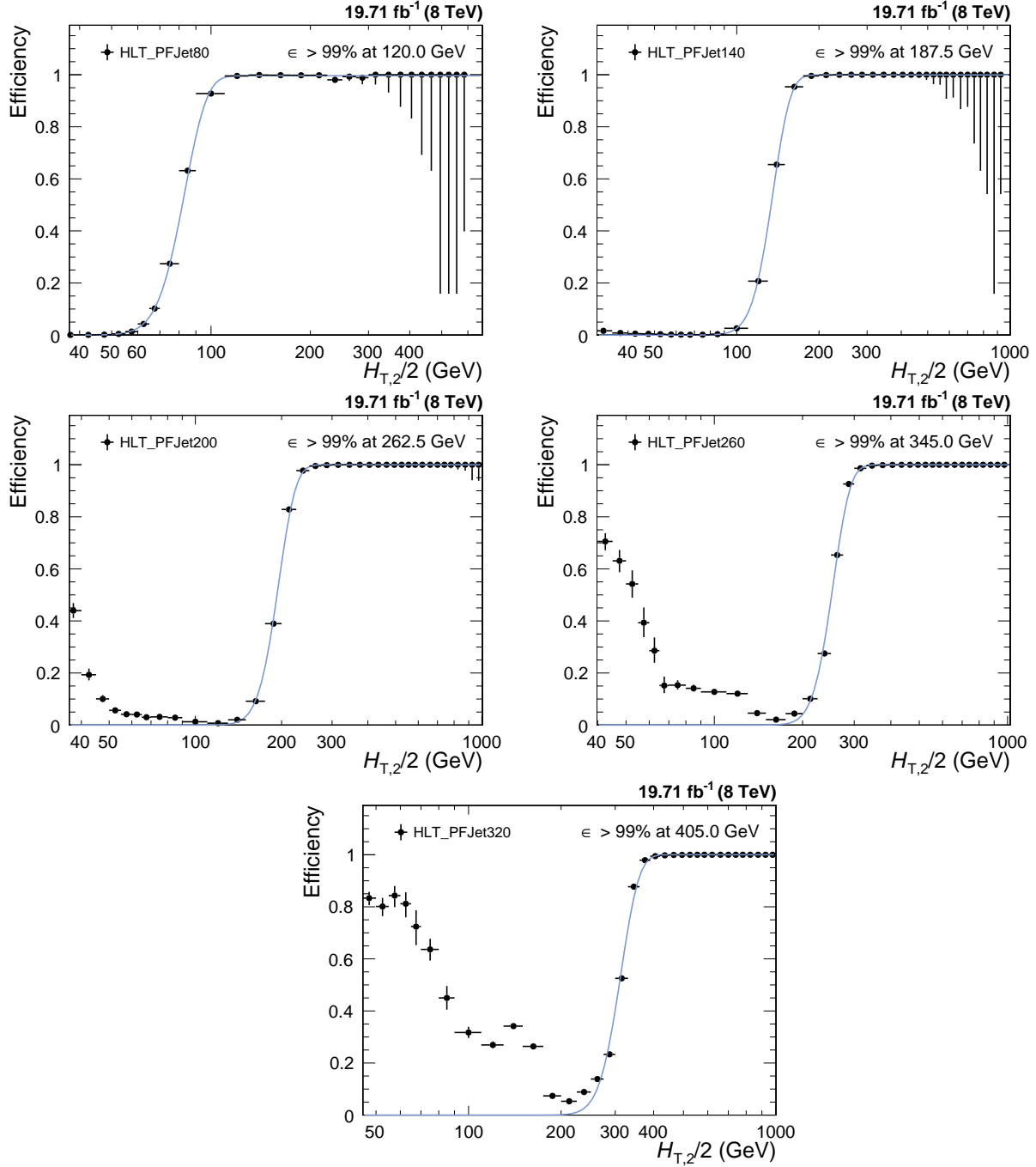


Figure 1.1: Trigger efficiencies turn-on curves for the single jet trigger paths used in the analysis. To determine the 99% efficiency threshold, the trigger turn-on curves are fitted using a sigmoid function (blue line), taking into account the uncertainties using Clopper-Pearson confidence intervals [1].

### 1.2.2 Primary Vertex Selection

A primary vertex (PV) is identified by a collection of tracks, measured in the tracker with a good fit quality between the hits and compatible with the beam line. The tracks are clustered according to the z-coordinate of their point of closest approach to the beam axis. Each event is required to have at least one good PV which is well reconstructed within a distance of  $|z(PV)| < 24$  cm to the nominal interaction point of the detector. Also the radial distance in x-y plane,  $\rho(PV)$  should be smaller than 2 cm. The number of degrees of freedom in vertex fit needs to be at-least four. Thus, at least four tracks must be present in order to perform a valid vertex fit.

### 1.2.3 Missing Transverse Energy

If all particles could be identified and perfectly measured, the transverse momentum of all particles would sum up to zero. Neutral weakly interacting particles, such as neutrinos, escape from typical collider detectors without producing any direct response in the detector elements. The presence of such particles must be inferred from the imbalance of total momentum of all visible particles. The vector momentum imbalance in the plane perpendicular to the beam direction is known as missing transverse momentum or energy ( $E_T^{\text{miss}}$ ). It is one of the most important observables for discriminating leptonic decays of W bosons and top quarks from background events which do not contain neutrinos, such as multijet and Drell–Yan events or searches for physics beyond the Standard Model which involve undetectable particles.

The ratio of missing transverse energy to the total transverse energy  $E_T^{\text{miss}}/\sum E_T$ , shown in Fig. 1.2 for  $n_j \geq 2$  (left) and  $n_j \geq 3$  (right), shows a discrepancy between data (black solid circles) and simulated MC (blue histogram), at the tail part of the distribution. This is because of a finite contribution from  $Z(\rightarrow \nu\bar{\nu}) + \text{jet}$  events which gives rise to non-zero  $E_T$  in the events in data. Such

events are absent in QCD simulated events in MC. Hence  $E_T^{\text{miss}}/\sum E_T$  is required to be less than 0.3 to reject events with high  $E_T^{\text{miss}}$ .

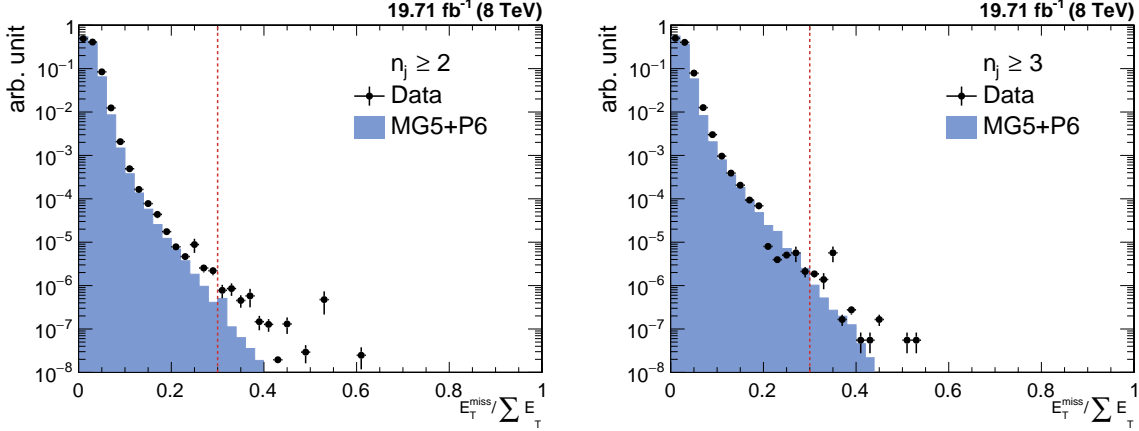


Figure 1.2: Missing transverse energy fraction of the total transverse energy per event in data (black solid circles) and simulated Monte Carlo events (blue histogram) in inclusive 2-jet (left) and 3-jet events (right). To remove background and noise, events with a fraction exceeding a certain threshold, here indicated with the red dashed line, are rejected.

### 1.2.4 Jet Identification

In order to suppress fake jets, arising from detector noise or misreconstructed particles, jet identification criteria (ID) has been applied. Instead of applying it event-wise, it is applied on each jet. The algorithm works on reconstructed jets using information of the clustered particle candidates. The official tight jet ID [7], recommended by JETMET group [2] is used. Due to pileup and electronic noise the jet constituent fractions may vary from event to event. In order to reject the noisy jets, some jet selection criteria are optimized to select only good quality jets. The selection criteria are implemented as selection cut on jet fractions. Table 1.4 summarizes the properties of the reconstructed jets and their respective cuts. Each jet should contain at least two particles, one of which should be a charged hadron. The cut on the fraction of neutral hadrons and photons removes HCAL noise and ECAL noise, respectively. Muons that are falsely identified and clustered as jets are removed by the muon fraction criterion. Based on information of the tracker, additional selec-

tion cuts are enforced in the region  $|\eta| < 2.4$ . The charged electromagnetic fraction cut removes the jets clustered from misidentified electrons. Furthermore, the fraction of charged hadrons in the jet must be larger than zero and jets without any charged hadrons are very likely to be pileup jets. The Figures 1.3 and 1.4 show the distributions of the jet constituents observed in data (black solid circles) and simulated MC events (blue histogram) for  $n_j \geq 2$  and  $n_j \geq 3$ , respectively.

Table 1.4: The jet ID removes noise and fake jets based on the properties of the reconstructed jets and the clustered particle candidates. All the selection cuts which are recommended by the JETMET group are applied [2].

Property		Loose ID	Tight ID
Whole $\eta$ region	neutral hadron fraction	$< 0.99$	$< 0.90$
	neutral EM fraction	$< 0.99$	$< 0.90$
	number of constituents	$> 1$	$> 1$
	muon fraction	$< 0.80$	$< 0.80$
only $ \eta  < 2.4$	charged hadron fraction	$> 0$	$> 0$
	charged multiplicity	$> 0$	$> 0$
	charged EM fraction	$< 0.99$	$< 0.90$

#### 1.2.4.1 Jet ID Efficiency

The efficiency of the jet ID as a function of  $H_{T,2}/2$  is studied using a tag-and-probe technique with dijet events. The two leading jets are required to be back-to-back in the azimuthal plane such that  $|\Delta\phi - \pi| < 0.3$ . One of the dijets is selected randomly as a “tag” jet which is required to fulfill the tight jet ID criteria. The other jet is called “probe” jet for which it is examined, whether it also passes the tight jet ID. The ID efficiency is defined as the ratio of events where the probe jet passes the ID requirements, over the total number of dijet events. Figure 1.5 shows the ID efficiency as a function of  $H_{T,2}/2$  for  $n_j \geq 2$  (left) and  $n_j \geq 3$  (right) ?. As expected, the jet ID efficiency is larger than 99%. The QCD cross section decreases as a function of  $H_{T,2}/2$  and hence the number of events decrease on moving to

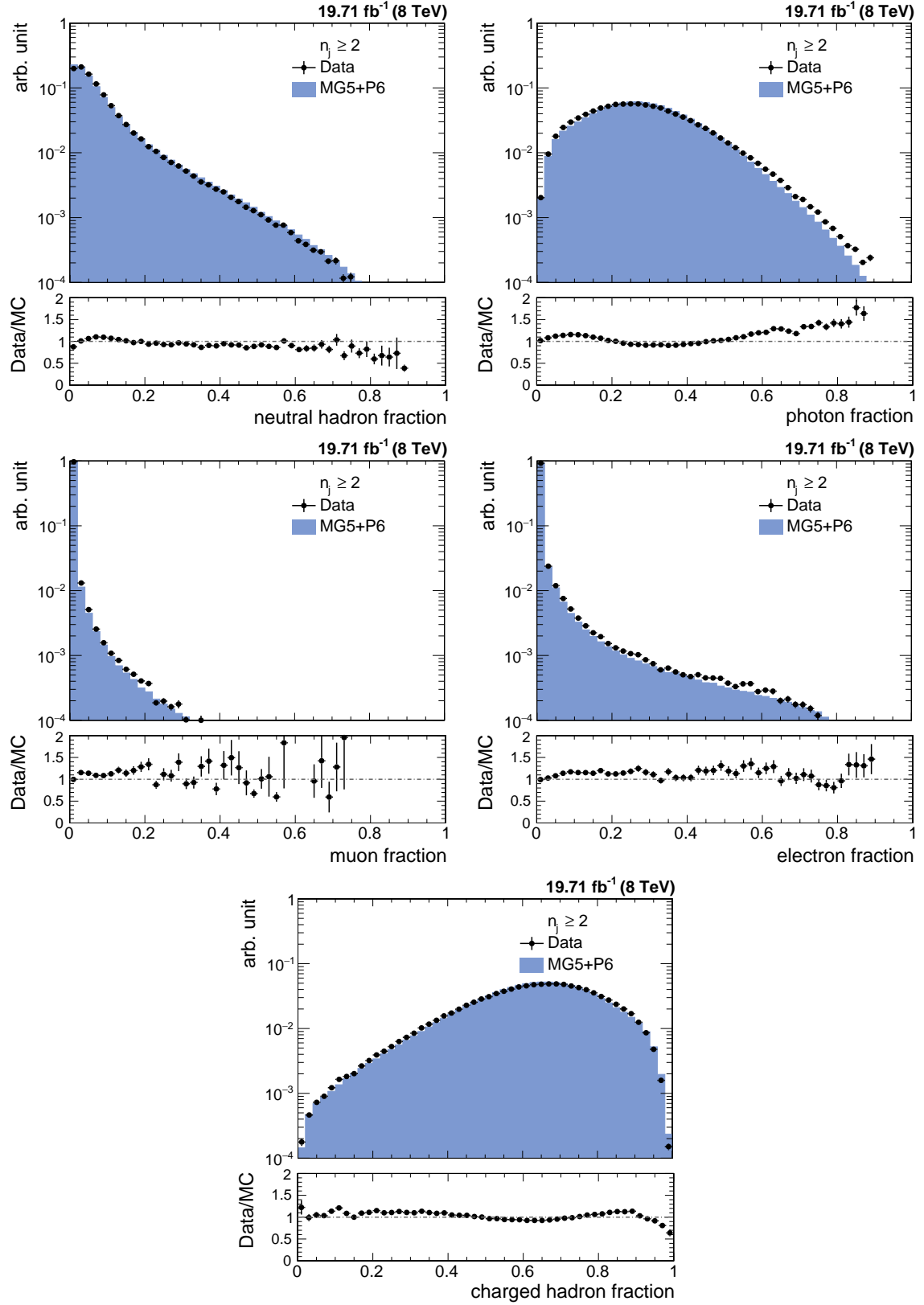


Figure 1.3: The fractions of jet constituents as observed in data (black solid circles) and simulated Monte Carlo events (blue histogram) for different types of PF candidates for inclusive 2-jet events. Data and simulations are normalized to the same number of events. The distributions are shown after the application of the jet ID.

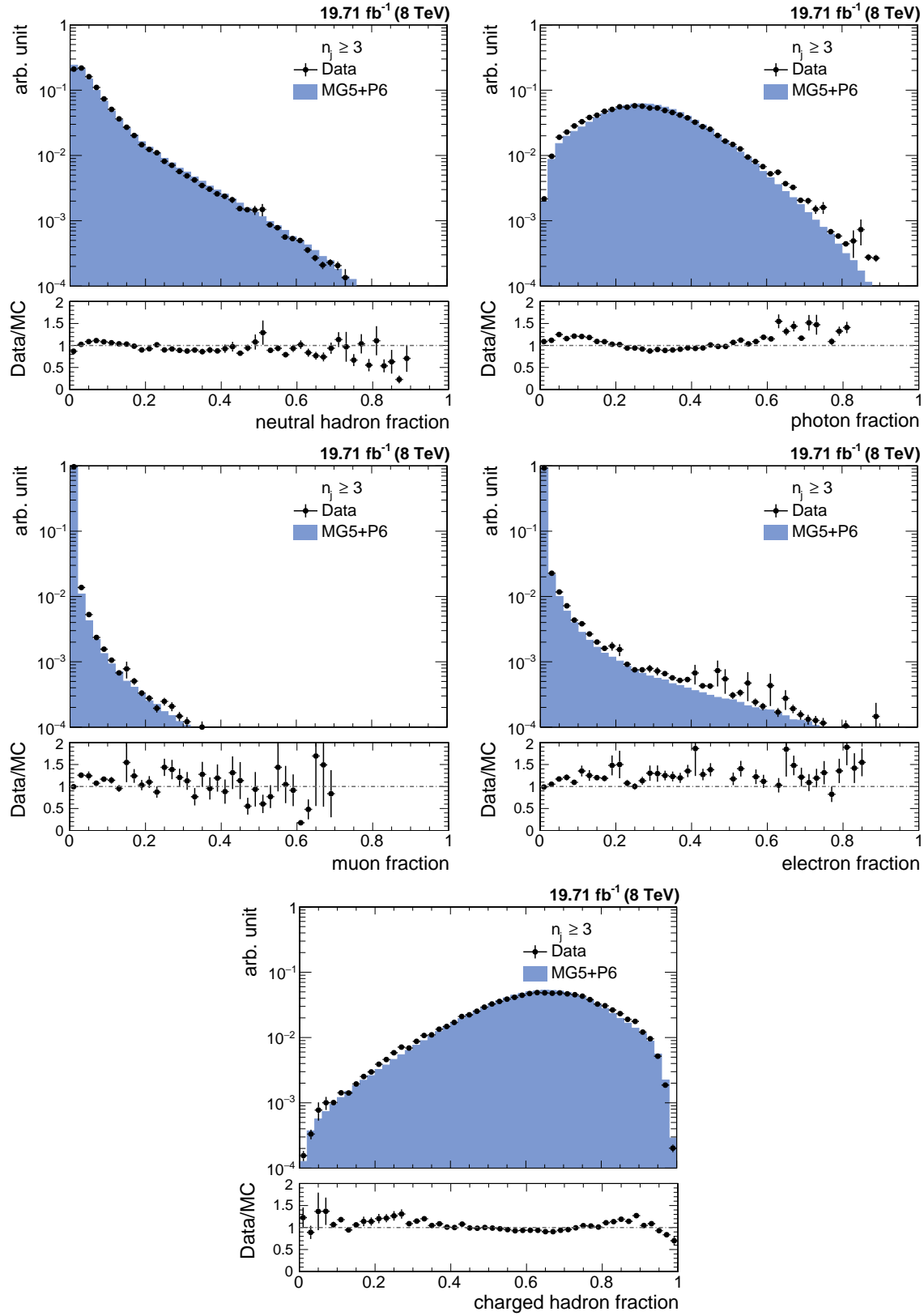


Figure 1.4: The fractions of jet constituents as observed in data (black solid circles) and simulated Monte Carlo events (blue histogram) for different types of PF candidates for inclusive 3-jet events. Data and simulations are normalized to the same number of events. The distributions are shown after the application of the jet ID.

higher  $H_{T,2}/2$ . Consequently the statistical fluctuations for ID efficiency are larger at higher  $H_{T,2}/2$ .

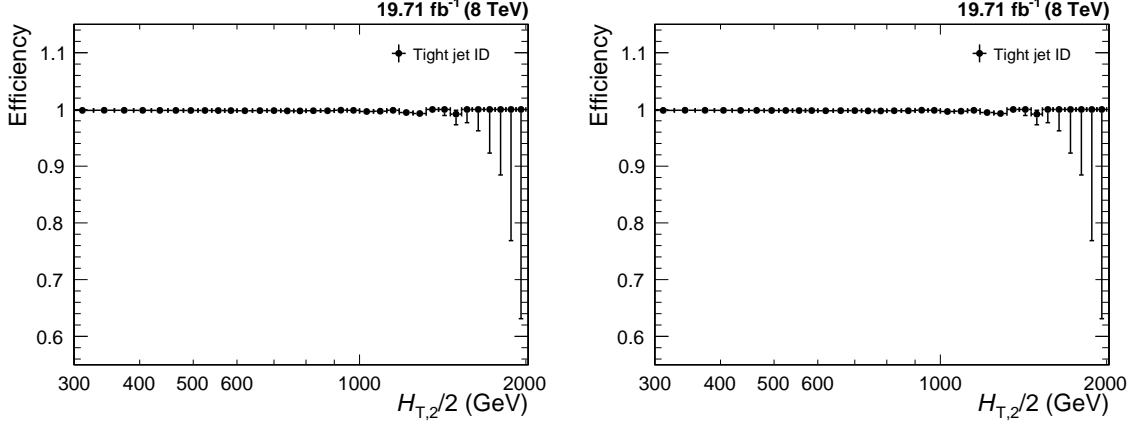


Figure 1.5: The jet ID efficiency studied using a tag-and-probe technique on dijet event topologies, is shown as a function of  $H_{T,2}/2$  for inclusive 2-jet (left) and 3-jet events (right) and it always exceeds 99%.

### 1.2.5 Jet Energy Corrections and Selection

The measurement presented in this thesis is based on jets clustered from PF candidates using the anti- $k_t$  jet algorithm with a size parameter of 0.7. All the jet energy corrections, described in Sec. [?](#) and recommended by CMS, are applied prior to this selection in order to have the correct energy scale of the jets. These comprises different correction levels for jets in data<sup>[2](#)</sup> and for jets in simulated events<sup>[3](#)</sup>. The jet selection, based on phase space cuts on transverse momentum and rapidity of jets in an event, is as follows :

- All jets having  $p_T > 150$  GeV and  $|y| < 5.0$  are selected.
- Events with at least two jets are selected.
- The two leading jets should have  $|y| < 2.5$  and further jets are counted only, if they lie within the same central rapidity range of  $|y| < 2.5$ .

<sup>2</sup>The JEC version applied on data is internally referred to as Winter14\_V8

<sup>3</sup>The latest JEC for run-independent Monte Carlo Samples are called START53\_V27

These cuts assure high detector acceptance and exactly same selection is applied in the measurement, simulated events as well in theoretical calculations for a consistent comparison.

## 1.3 Comparison with Simulated Events

### 1.3.1 Pile-up Reweighting

The official Monte-Carlo samples are generated with distributions for the number of pileup interactions which is meant to roughly cover the conditions expected for each data-taking period. But the number of pile-up events implemented in the simulation  $N_{\text{MC}}(N_{\text{PU,truth}})$ , is not exactly the same as the one measured in data  $N_{\text{data}}(N_{\text{PU,est.}})$ . To match the pile-up distributions in data and simulated events, the simulated events are reweighted with a weight  $w_{\text{PU}}$ , given by :

$$w_{\text{PU}} = \frac{N_{\text{data}}(N_{\text{PU,est.}}) / \sum N_{\text{data}}}{N_{\text{MC}}(N_{\text{PU,truth}}) / \sum N_{\text{MC}}} \quad (1.5)$$

Figure 1.6 shows the number of reconstructed vertices before (left) and after reweighting (right). The significant mismatch of the pile-up distributions in data (black solid circles) and simulated MC events (blue histogram), which is present before the reweighting, completely vanishes.

### 1.3.2 Cross Section Comparison

The measured data distribution of differential cross section at detector level is compared to the predictions of Monte Carlo simulation using MADGRAPH5 generator interfaced with PYTHIA6 (MG5+P6) and including the detector simulation as well as to a fixed-order prediction of NLOJET++. Figure 1.7 shows the comparison of differential cross section as a function of  $H_{\text{T},2}/2$  for  $n_{\text{j}} \geq 2$  (left) and  $n_{\text{j}} \geq 3$  (right),



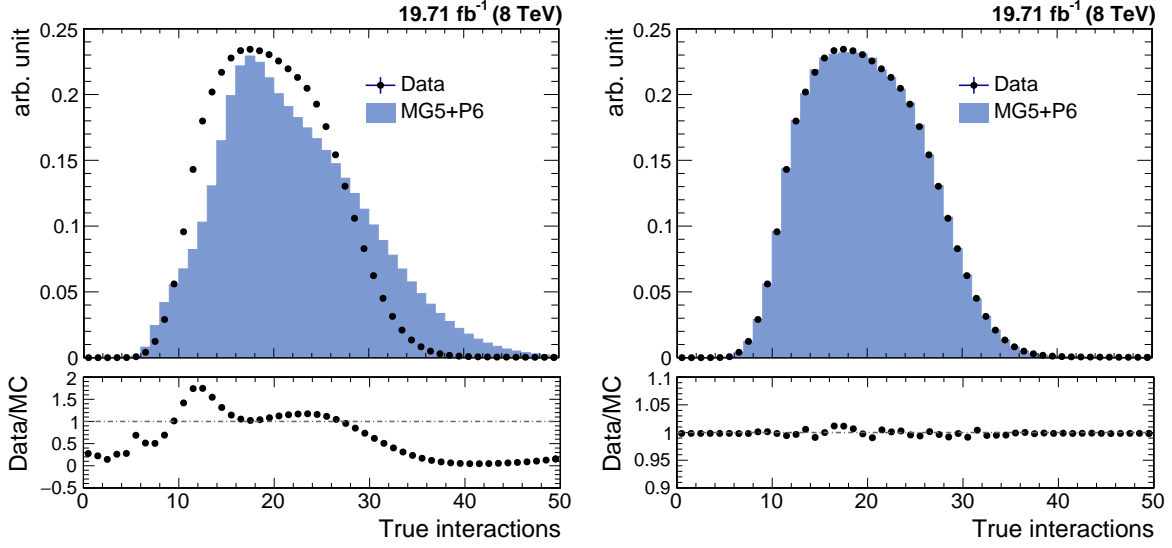


Figure 1.6: Number of reconstructed vertices in data (black solid circles) and simulated Monte Carlo events (blue histogram) before (left) and after (right) the pile-up reweighting.

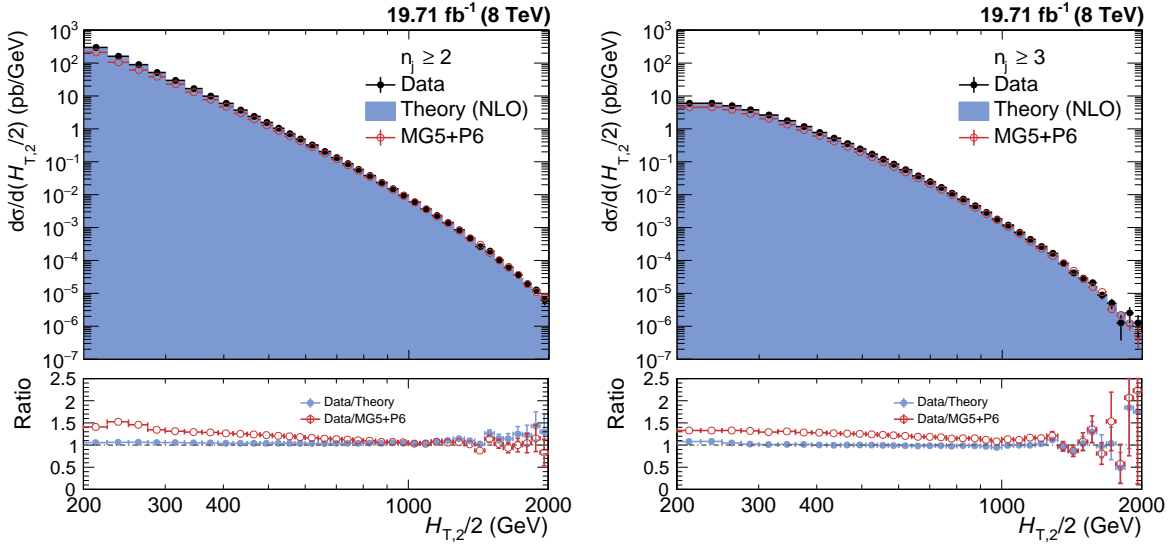


Figure 1.7: The differential cross sections are compared for data (black solid circles) and LO MADGRAPH5 + PYTHIA6 (MG5+P6) Monte Carlo (red empty circles), at reconstructed level with NLO theory predictions (blue histogram), as a function  $H_{T,2}/2$  for inclusive 2-jet events (left) and 3-jet events (right). Ratios of data to the Monte Carlo predictions (red line) as well as to the NLO predictions (blue line) are shown in bottom panel of each plot.

for data (black solid circles), MG5+P6 MC (red empty circles) and NLO (blue histogram). The bottom panel in each plot shows the ratio of data to the MC predictions (red line) as well as to the NLO predictions (blue line). The NLO predictions

on parton level are not corrected for non-perturbative effects. Still the NLO predictions describe the data better as compared to the LO MC simulations. The sufficient data for  $n_j \geq 2$  and  $n_j \geq 3$  events are available up to  $H_{T,2}/2 = 2$  TeV and 1.68 TeV, respectively. As mentioned in Sec. ? that the minimum kinematical cut on  $H_{T,2}/2$  is 300 GeV. Hence the observable is studied in the range  $300 \text{ GeV} \leq H_{T,2}/2 < 2$  TeV for  $n_j \geq 2$  and  $300 \text{ GeV} \leq H_{T,2}/2 < 1.68 \text{ TeV}$  for  $n_j \geq 3$  events.

## 1.4 Jet Energy Resolution (JER)

In an ideal experiment, the value of a physical quantity would be determined exactly with an infinite precision. For e.g. whenever a particle with energy  $E$  passes an ideal calorimeter having infinite resolution, the measured energy should always be equal to  $E$ . But in real detector, the measured energy of the above mentioned particle might differ from the value  $E$ . This shift of the measured quantity from its true value may be due to detector noise, uncertainties in the calibration, non-linearity of the response etc. Hence this results in the finite value of the detector resolution (JER). In such case, the measured values of energy of different particles, crossing the same detector with same energy  $E$ , will be different. The set of measurements of this type would in the form of a gaussian distribution, centered around the true value of the measured quantity, whose width is generally interpreted as detector resolution. The resolution of a detector indicates that how precise it is able to measure a given physical observable. The narrower the distribution, the higher the resolution is and hence the more precise is the detector. The importance of the measurement of the detector resolution lies in the fact that it indicates how much the measured value of the observable differs from the true one.

Due to finite resolution of the CMS detector, the measured transverse momentum of jets gets smeared. Since the observable in this study i.e.  $H_{T,2}/2$  is the average sum of transverse momentum of leading and sub-leading jets, the resolu-

tion of the detector has to be studied in terms of the observable. CMS detector simulation based on MG5+P6 MC event generators is used to determine the resolution as both the particle and reconstructed level information is available. The jets clustered from stable generator particles called Gen jets as well as from particle flow candidates reconstructed from the simulated detector output called Reco jets, are used. The studies of the JETMET working group at CMS has shown that the jet energy resolution in data is actually worse than in simulation [3]. So the reconstructed jet transverse momentum needs to be smeared additionally to match the resolution in data. Table 1.5 shows the scaling factors ( $c$ ) which need to be applied on the transverse momentum of simulated reconstructed jets. The scaling factors depend on the absolute  $\eta$  of the jet. The uncertainty on these measured scaling factors needs to be taken into account in a physics analysis. This is done by smearing the reconstructed jets with two additional sets of scaling factors,  $c_{up}$  and  $c_{down}$ , that correspond to varying the factors up and down respectively, by one sigma and evaluating the impact of these new sets.

Table 1.5: JETMET working group at CMS has shown that the jet energy resolution in data is actually worse than in simulation [3]. The scaling factors need to be applied to the reconstructed jet transverse momentum in simulated events to match the resolution in data. The uncertainty on the resolution is given by an upwards and downwards variation  $c_{up}$  and  $c_{down}$  of the smearing factor  $c_{central}$ .

$\eta$	0.0 – 0.5	0.5 – 1.1	1.1 – 1.7	1.7 – 2.3	2.3 – 2.8
$c_{central}$	1.079	1.099	1.121	1.208	1.254
$c_{down}$	1.053	1.071	1.092	1.162	1.192
$c_{up}$	1.105	1.127	1.150	1.254	1.316

The reconstructed jet  $p_T$  is smeared randomly using a gaussian width widened by the scaling factor ( $c_{central}$ )

$$p_T \rightarrow Gauss\left(\mu = p_T, \sigma = \sqrt{c_{central}^2 - 1} \cdot JER(p_T)\right) \quad (1.6)$$

where  $JER(p_T)$  is the resolution determined as a function of jet  $p_T$  using

MG5+P6 MC simulated events. After smearing transverse momentum of each reco jet,  $H_{T,2}/2$  is calculated from both generator particle jets (Gen  $H_{T,2}/2$ ) as well as the particle flow or reconstructed jets (Reco  $H_{T,2}/2$ ). Then the response is calculated as defined in the Eq. 1.7.

$$R = \frac{\text{Reco } H_{T,2}/2}{\text{Gen } H_{T,2}/2} \quad (1.7)$$

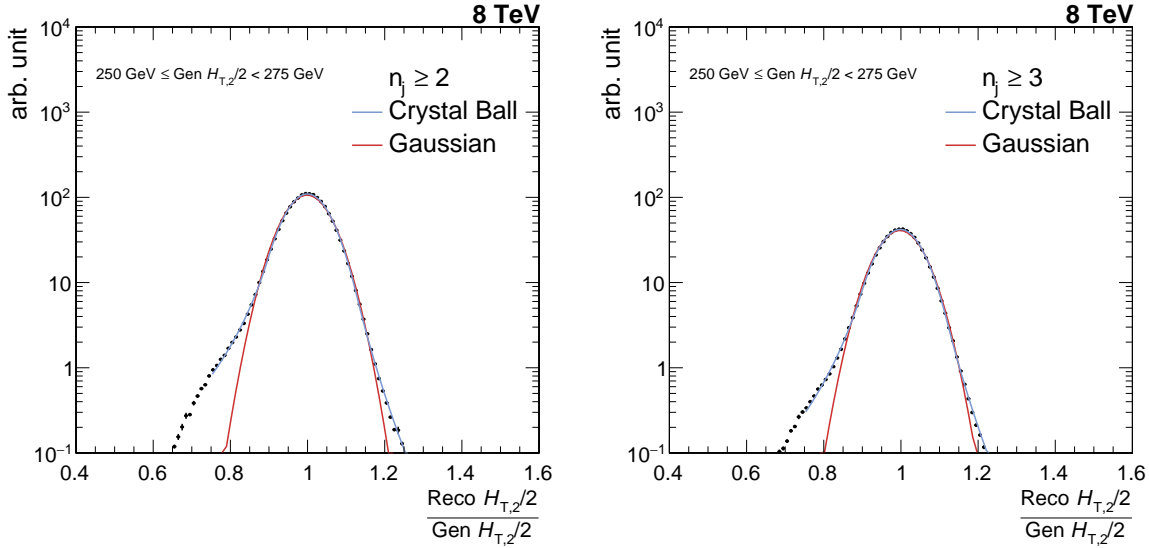


Figure 1.8: Fitting of the resolution distribution as a function of  $H_{T,2}/2$  for inclusive 2-jet (left) and for inclusive 3-jet events (right). The blue line shows the double-sided Crystal Ball function fit of  $\frac{\text{Reco } H_{T,2}/2}{\text{Gen } H_{T,2}/2}$  in each Gen  $H_{T,2}/2$  bin, overlayed by Gaussian fitting the core of the resolution (red line).

The width of the response distribution in a given Gen  $H_{T,2}/2$  bin is interpreted as the resolution which can in good approximation be described by the  $\sigma$  of a Gaussian fit to the core of distribution. To take into account the non-Gaussian tails of the jet response distribution, a double-sided Crystal-Ball function is used. The resolution as a function of  $H_{T,2}/2$  is calculated separately for both  $n_j \geq 2$  and  $n_j \geq 3$  events. A fit example for one Gen  $H_{T,2}/2$  bin is shown in Fig. 1.8 for  $n_j \geq 2$  (left) and inclusive 3-jet events (right). Here the black dots represent the jet response distribution and the double-sided Crystal-Ball fit (blue line) is overlayed by the Gaussian fit (red line). The resolution in each Gen  $H_{T,2}/2$  bin is then plotted

as a function of  $\text{Gen } H_{T,2}/2$ . As expected, it has been observed from Fig. 1.9 that as compared to Gaussian function fit (red solid circles), the Crystal Ball function (blue solid circles) better describes the measured distributions, especially in the low- $H_{T,2}/2$  region where the non-Gaussian tails are more pronounced. Hence the Crystal Ball function is preferred to determine the resolution.

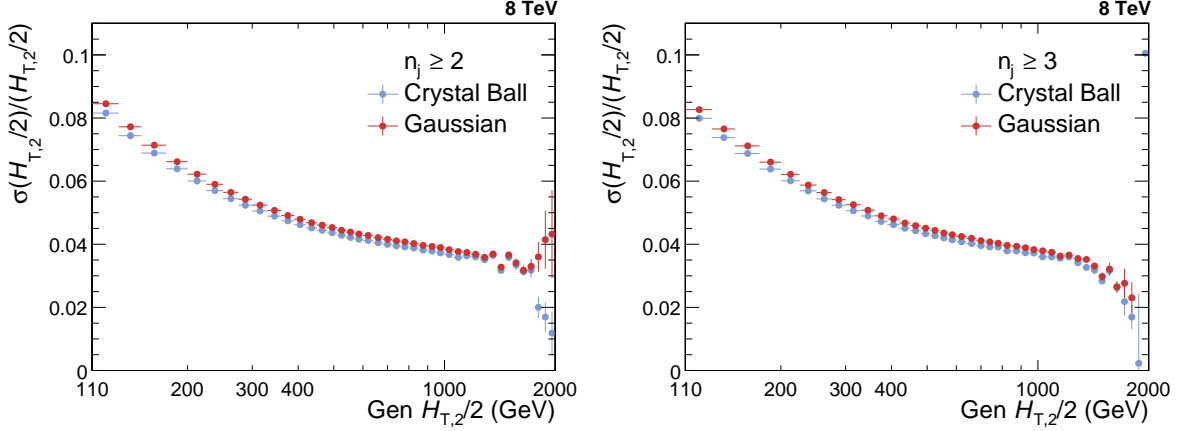


Figure 1.9: Comparison of jet energy resolution calculated using Crystal-Ball fit function (blue solid circles) and Gaussian fit function (red solid circles) for inclusive 2-jet events (left) and for inclusive 3-jet events (right).

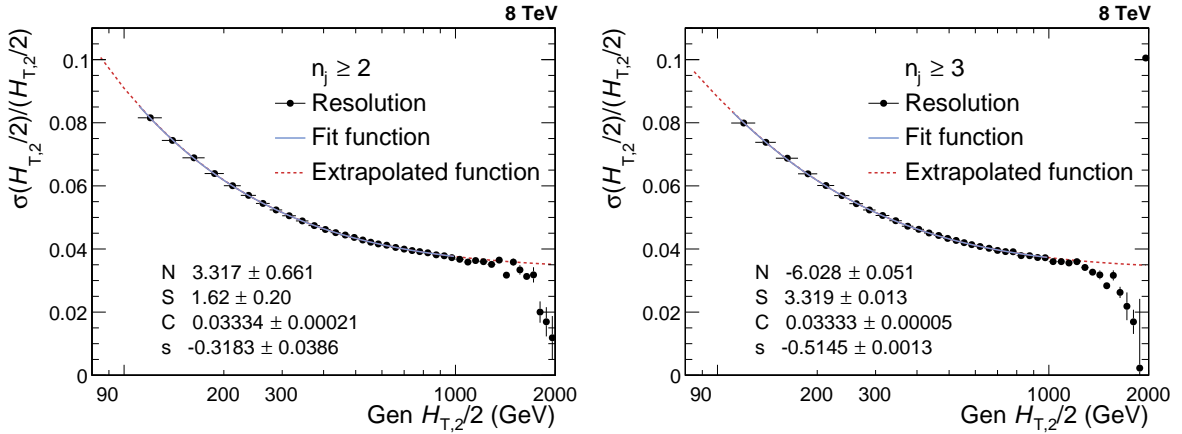


Figure 1.10: Jet energy resolution (JER) is shown as a function of  $\text{Gen } H_{T,2}/2$  for inclusive 2-jet events (left) and for inclusive 3-jet events (right). JER (black solid circles) is fitted by using the modified NSC-formula (blue solid line) which is extrapolated to 80 GeV and upto 2 TeV (red dashed line) to consider the migration into lower as well as higher bins.

Figure 1.10 shows the final relative jet energy resolution (JER) which is described by a modified version of the NSC formula (blue solid line) [8], as mentioned

in Equation 1.8. To consider the migration to lower as well higher bins and to obtain the resolution with reasonable statistics over the full range of Gen  $H_{T,2}/2$ , the fit function is extrapolated to 80 GeV and upto 2 TeV which is shown by red dashed line. The fit formula used here is based on the usual NSC formula which describes the resolution in terms of noise  $N$  originating due to electronic and pileup noise and is independent of  $H_{T,2}/2$ ; a stochastic component  $S$  due to sampling fluctuation and EM fraction fluctuation per hadrons; and a constant term  $C$  because of dead material, magnetic field and calorimeter cell to cell fluctuation. In the low  $H_{T,2}/2$  region the tracking has a non-negligible influence on the resolution due to the particle flow algorithm, so the additional parameter  $s$  is introduced to obtain slightly better fits. The parameters obtained after fitting the relative resolution using the above mentioned NSC formula are tabulated in Table 1.6 for  $n_j \geq 2$  and  $n_j \geq 3$  events. This calculated JER is used in unfolding procedure to smear the generated truth spectrum which is used as input in getting the response matrices and is explained in details in Sec. 1.5.1.

$$\frac{\sigma(x)}{x} = \sqrt{sgn(N) \cdot \frac{N^2}{x^2} + S^2 \cdot x^{s-1} + C^2} \quad (1.8)$$

Table 1.6: The parameters obtained by fitting the relative resolution as a function of  $H_{T,2}/2$ , using the modified NSC formula, for inclusive 2-jet and inclusive 3-jet events.

	N	S	C	s
Inclusive 2-jet	3.32	1.62	0.0333	-0.318
Inclusive 3-jet	-6.03	3.32	0.0333	-0.515

Since the JER is calculated using MG5+P6 Reco and Gen  $H_{T,2}/2$  distributions, so it is expected that if Gen  $H_{T,2}/2$  is smeared using this JER, it should match the Reco  $H_{T,2}/2$ . But this extracted JER in one large rapidity bin, smears the Gen  $H_{T,2}/2$  too much because Smeared Gen/Gen ratio (red line) shows a discrepancy from simulated Reco/Gen ratio (blue line), as observed in Fig. 1.11 for  $n_j \geq 2$  (left)

and  $n_j \geq 3$  (right). When the 30% reduced JER is used to smear Gen, then the ratio Smeared Gen/Gen (pink line) matches with simulated Reco/Gen ratio (blue line) within the statistical fluctuations. Hence an additional unfolding uncertainty is attributed by comparison to 30% reduced JER for both  $n_j \geq 2$  and  $n_j \geq 3$  events. Due to high statistical fluctuations at high  $H_{T,2}/2$ , range is presented upto 1.68 TeV only.

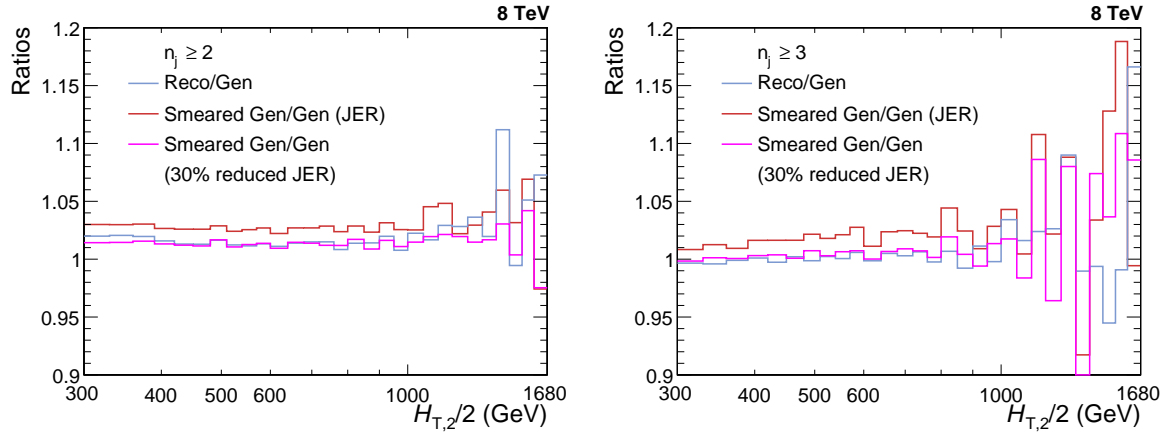


Figure 1.11: MADGRAPH5 + PYTHIA6 Gen smeared using extracted jet energy resolution (JER) shows a discrepancy from simulated Reco as Smeared Gen/Gen ratio (red line) does not match with Reco/Gen ratio (blue line), for both inclusive 2-jet (left) and inclusive 3-jet events (right). Smeared Gen/Gen ratio (pink line) where Gen is smeared using 30% reduced JER matches with simulated Reco/Gen ratio (blue line) within the statistical fluctuations. Hence an additional unfolding uncertainty is attributed by comparison to 30% reduced JER.

## 1.5 Unfolding

One of the main goals in an experimental measurement is to do the comparison between data and theory predictions or with the results from other experiments. But the finite detector resolution and the steeply falling jet  $p_T$  spectrum distorts the physical quantities. As a result, the measured observables are different from the corresponding true values. Each  $p_T$  bin content contains the migrated events from neighbouring bins along with the original events. So an unfolding process of the data should be followed in order to remove detector effects. In this analysis, the measured

cross sections are corrected for detector smearing effects and unfolded to stable particle level by using the iterative D'Agostini Bayesian method [9], implemented in the RooUnfold software package [10]. The unfolding process is regularized by the number of iteration steps in this algorithm. A higher number of iterations yields a reduced  $\chi^2$  but also increases the uncertainty and introduces larger bin-by-bin fluctuations and correlations. The regularization is optimized using simulated events and best results with low bin-by-bin correlations and low  $\chi^2$  are achieved using four iterations in the unfolding algorithm.

### 1.5.1 Response matrices

Unfolding uses a response matrix as an input that maps the true distribution onto the measured one. The response matrix is usually derived from simulated Monte Carlo (MC) samples, which uses as input the true distribution from MC and introduces the smearing effects by taking into account the detector resolution. Then this response matrix is used to unfold the measured data spectrum. But there are several drawbacks of constructing response matrix using this method. In some phase space regions, the shape of the distribution is not well described by the LO predictions. Also, the number of events in the MC samples are limited at high transverse momenta which introduces non-negligible statistical fluctuations in the response matrix.

However, there is an indirect way of constructing the response matrix which uses a custom Toy Monte Carlo method. In this method, the particle level or true  $H_{T,2}/2$  spectrum is obtained by fitting the theoretically predicted NLO spectrum. Then this distribution is smeared with forward smearing technique, using the extracted jet energy resolution (JER) to obtain the reconstructed level or measured  $H_{T,2}/2$  spectrum. After that, the response matrix is constructed from these two distributions is used for the unfolding procedure.



The NLO spectrum obtained from CT10-NLO PDF set is fitted with the following two different functions defined in Eq. 1.9 and 1.12. These functions describes both the normalization and shape of the distribution.

• **Function I :**

$$f(H_{T,2}/2) = N[x_T]^{-a}[1 - x_T]^b \times \exp[-c/x_T] \quad (1.9)$$

where N is normalization factor and a, b, c are fit parameters.

This function is derived from the below function [11] :

$$f(p_T; \alpha, \beta, \gamma) = N_0[p_T]^{-\alpha} \left[ 1 - \frac{2 p_T \cosh(y_{min})}{\sqrt{s}} \right]^\beta \times \exp[-\gamma/p_T] \quad (1.10)$$

using

$$\alpha = a, \quad \beta = b, \quad \gamma = c * \sqrt{s}/2, \quad x_T = \frac{2 * H_{T,2}/2 * \cosh(y_{min})}{\sqrt{s}} = \frac{2 * H_{T,2}/2}{\sqrt{s}} \quad (1.11)$$

where transverse scaling variable  $x_T$  corresponds to the proton fractional momentum  $x$  for dijets with rapidity  $y = 0$ ,  $\sqrt{s} = 8000$  GeV and  $y_{min}$  is low-edge of the rapidity bin  $y$  under consideration (here  $y_{min}$  is taken equal to 0)

• **Function II :**

$$f(H_{T,2}/2) = A_0 \left( 1 - \frac{H_{T,2}/2}{A_6} \right)^{A_7} \times 10^{F(H_{T,2}/2)}, \text{ where } F(x) = \sum_{i=1}^5 A_i \left( \log\left(\frac{x}{A_6}\right) \right)^i \quad (1.12)$$

where the parameter  $A_6$  is fixed to  $\frac{\sqrt{s}}{2 \cosh(y_{min})}$ , where  $\sqrt{s} = 8000$  GeV and  $y_{min}$  is the minimum rapidity. The other parameters are derived from the fitting.

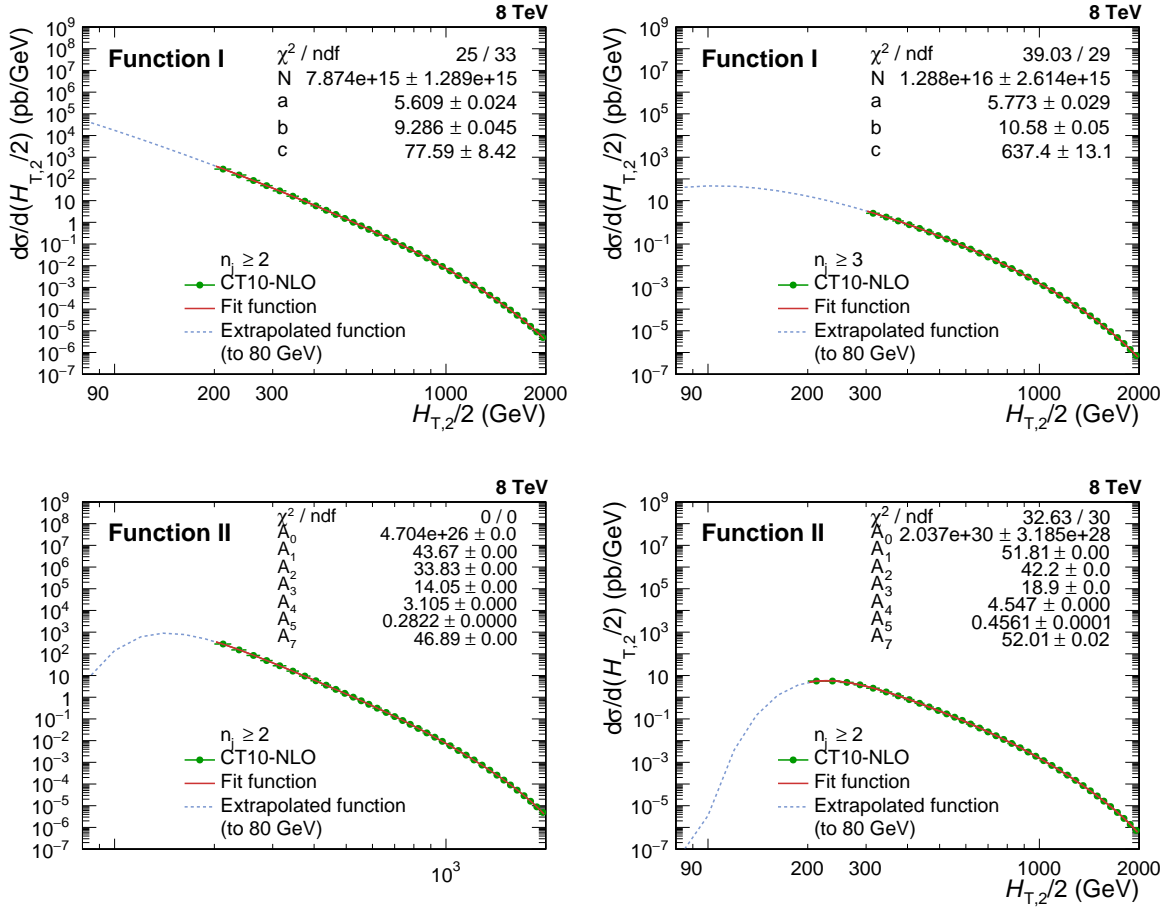


Figure 1.12: Fitted CT10-NLO spectrum of differential cross section as a function of  $H_{T,2}/2$  (green solid circles) using Function I (top) defined in Eq. 1.9 and using Function II (bottom) given by Eq. 1.12, for inclusive 2-jet events (left) and for inclusive 3-jet events (right). To consider the migration to lower  $H_{T,2}/2$  bins, the fit functions described by red lines are extrapolated to 80 GeV (blue dashed lines).

Figure 1.12 shows the fitted CT10-NLO spectrum of differential cross section as a function of  $H_{T,2}/2$  (green solid circles) using Function I (top) and using Function II (bottom) : for inclusive 2-jet events (left) and for inclusive 3-jet events (right). Function I is used primarily to generate response matrices and perform the closure tests and Function II is used as an alternative function to calculate unfolding uncertainty, described in Sec. 1.6.4. To include the migration to lower bins, the fit functions described by red lines are extrapolated to 80 GeV (blue dashed lines).

A flat  $H_{T,2}/2$  spectrum is generated by using toy Monte Carlo events and the fit parameters obtained from the NLO spectrum using function I (as shown in Fig. 1.12)

provides weights to the flat spectrum. A total of ten million events are generated randomly (in  $H_{T,2}/2$  range 80-2000). These generated values are then smeared with a Gaussian function, where  $\sigma$  of the Gaussian is determined from the relative resolution parametrization as a function of  $H_{T,2}/2$  calculated from NSC formula mentioned in equation 1.8. The parameters N, S, C used for smearing are taken from Table 1.6. These randomly generated ( $\text{Gen}_{\text{Toy}}$ ) and smeared ( $\text{Measured}_{\text{Toy}}$ ) values are used to fill the response matrices. Figure 1.13 shows the response matrices derived using the Toy MC for  $\eta_j \geq 2$  (left) and  $\eta_j \geq 3$  events (right). The matrices are normalized to the number of events in each column. The response matrices are diagonal with small off-diagonal migrations between close-by  $H_{T,2}/2$  bins.

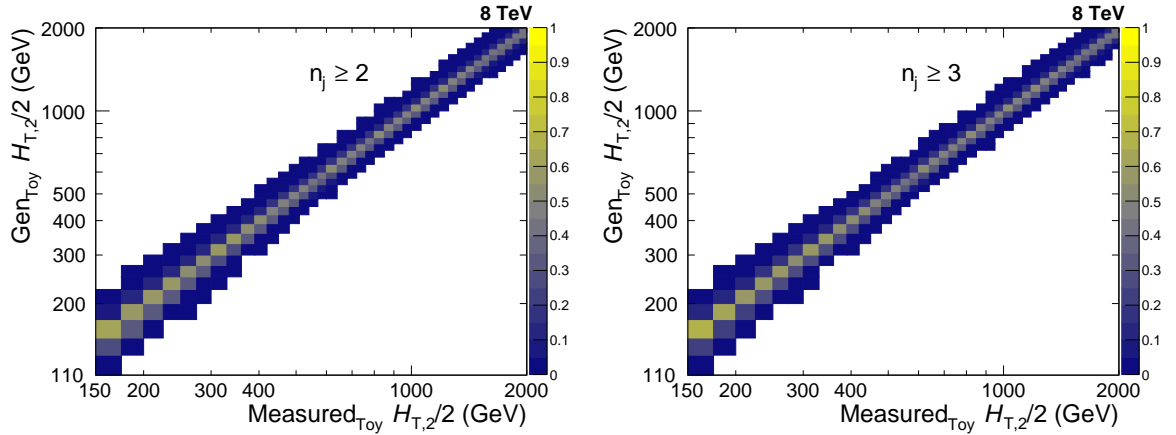


Figure 1.13: The response matrices are derived using the Toy Monte Carlo and forward smearing method, for inclusive 2-jet (left) and inclusive 3-jet events (right). The matrices are normalized to the number of events in each column and are diagonal with small off-diagonal migrations between close-by  $H_{T,2}/2$  bins.

### 1.5.2 Closure test

A closure test has been performed to confirm the working of the unfolding procedure. In this test,  $\text{Measured}_{\text{Toy}}$  spectrum is unfolded using the constructed response matrices shown in Figure 1.13. It is expected that the same  $\text{Gen}_{\text{Toy}}$  spectrum should be re-obtained after unfolding. Figure 1.14 shows that the unfolded  $\text{Measured}_{\text{Toy}}$  spectrum, matches exactly with  $\text{Gen}_{\text{Toy}}$  spectrum as the ratio of these distributions

is perfectly flat at one for both  $n_j \geq 2$  (left) and  $n_j \geq 3$  events (right).

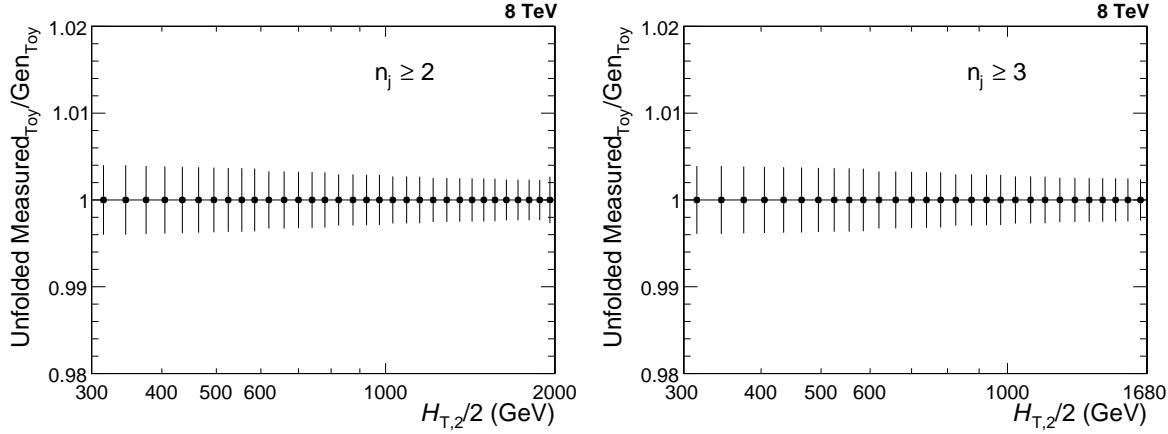


Figure 1.14: Closure test of the unfolding technique where the smeared spectrum obtained from Toy Monte Carlo method (Measured<sub>Toy</sub>), is unfolded using the constructed response matrices (obtained by forward smearing the randomly generated spectrum (Gen<sub>Toy</sub>) using extracted jet energy resolution (JER)). As expected, the unfolded Measured<sub>Toy</sub> spectrum matches exactly with Gen<sub>Toy</sub> spectrum as the ratio of these distributions is perfectly flat at one for both  $n_j \geq 2$  (left) and  $n_j \geq 3$  events (right).

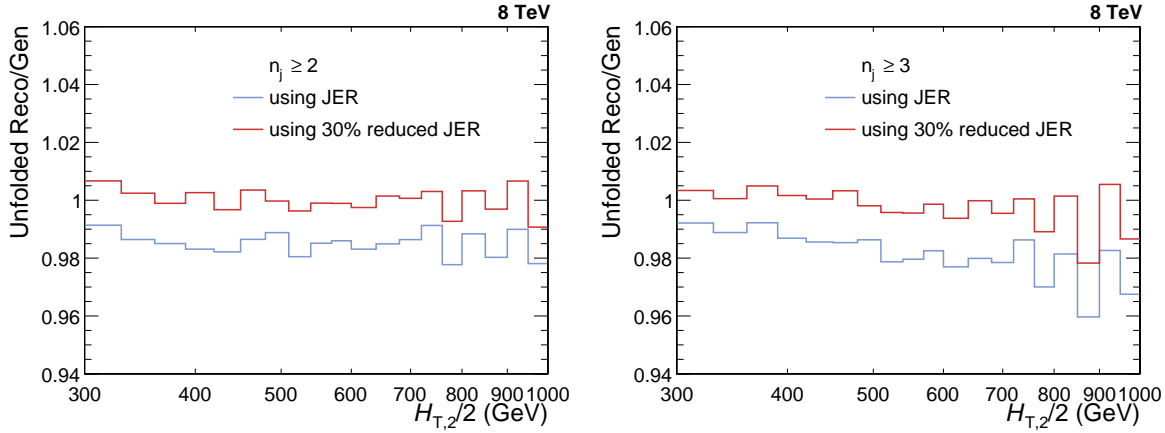


Figure 1.15: Reco MADGRAPH5 + PYTHIA6 Monte Carlo (MG5+P6 MC) differential cross section distributions unfolded with the response matrices (obtained by forward smearing the randomly generated spectrum (Gen) using extracted jet energy resolution (JER)), does not give a good closure with Gen MG5+P6 MC (blue line), for inclusive 2-jet (left) and inclusive 3-jet events (right). After performing the unfolding using 30% reduced JER, a good closure is obtained (red line).

For another closure test, Reco MG5+P6 MC differential cross section distribution is unfolded using the above constructed response matrices using JER for forward smearing the randomly generated spectrum. While taking ratio of the un-

folded distribution to that of Gen MG5+P6 MC, it is observed that a well closure is not obtained. This is represented by blue line in Fig. 1.15 for  $n_j \geq 2$  (left) and  $n_j \geq 3$  (right). As observed in Fig. 1.11 in Sec. 1.4, if Reco MG5+P6 MC is unfolded using the response matrices obtained using 30% reduced JER, then the good closure is obtained as shown by red line in Fig. 1.15.

### 1.5.3 Unfolding measurement

After validity the unfolding method, the measured differential cross sections as a function of  $H_{T,2}/2$  are unfolded using the above reconstructed response matrices. The unfolded data spectrum is compared to that of measured one in Fig. 1.16 for  $n_j \geq 2$  (left) and  $n_j \geq 3$  (right). As already discussed that 30% reduced JER gives better closures than JER, so the unfolding of data is done with response matrices using JER (blue solid circles) as well as 30% reduced JER (red solid circles). The difference between both is taken as an additional uncertainty on the unfolded measurement.

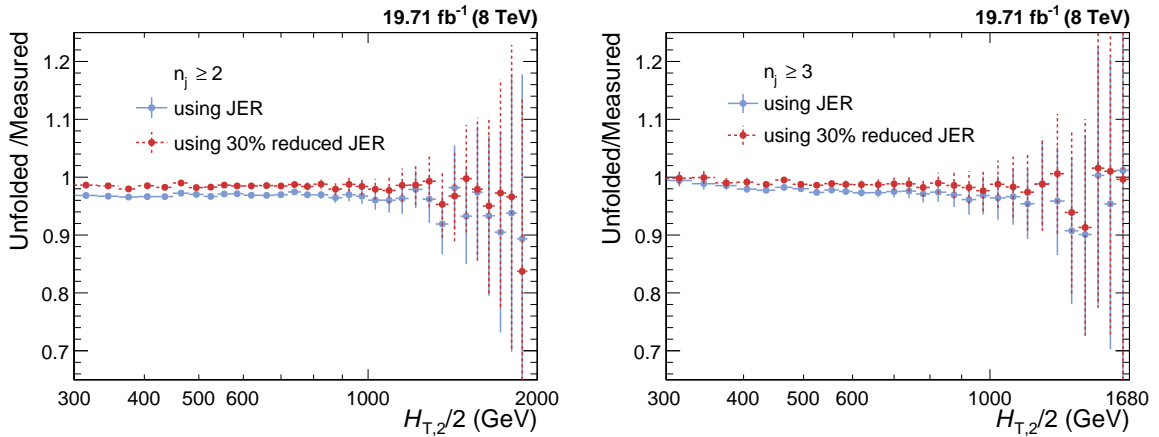


Figure 1.16: The unfolded differential cross sections as a function of  $H_{T,2}/2$  are compared with that of the measured one for inclusive 2-jet (left) and inclusive 3-jet events (right). The unfolding is done with response matrices using JER (blue solid circles) as well as 30% reduced JER (red solid circles). The difference between both is taken as an additional uncertainty on the unfolded measurement.

## 1.6 Experimental uncertainties

In an experimental measurement of any physical observable, the uncertainties play a key role and hence are important to study in a physics analysis. The uncertainties are of two types : statistical and systematic. The statistical uncertainties arise due to random fluctuations depending on the number of selected events. The systematic uncertainties may be due to known detector effects, model dependence, assumptions made or various corrections applied. The statistical and systematic errors can in general be added in quadrature, if uncorrelated. In this section, all the experimental uncertainties affecting the cross section measurement are described.

### 1.6.1 Luminosity measurement uncertainty

The LHC luminosity delivered to CMS in the 2012 proton-proton physics run is measured by using the silicon pixel cluster counting method [12]. The uncertainty related to the integrated luminosity measurement for the 2012 LHC run is estimated to be 2.5% (syst.) and 0.5% (stat.). The luminosity uncertainty propagates directly to any absolute cross section measurement. Hence, a combined systematic uncertainty of 2.6% is assigned which is fully correlated across all the  $H_{T,2}/2$  bins.

### 1.6.2 Statistical uncertainty

Statistical uncertainty on the measurement is propagated through the unfolding procedure using a toy MC technique. The measured data points are smeared within their statistical uncertainties and the unfolding is repeated multiple times for each smeared spectra. One million of such toy spectra are used to propagate the statistical uncertainty. The statistical uncertainty slightly increases during the unfolding process which can be seen in Fig. 1.17 where the relative statistical uncertainty before (blue line) and after (red line) unfolding procedure is shown for  $n_j \geq 2$  (left) and  $n_j \geq 3$  events (right).

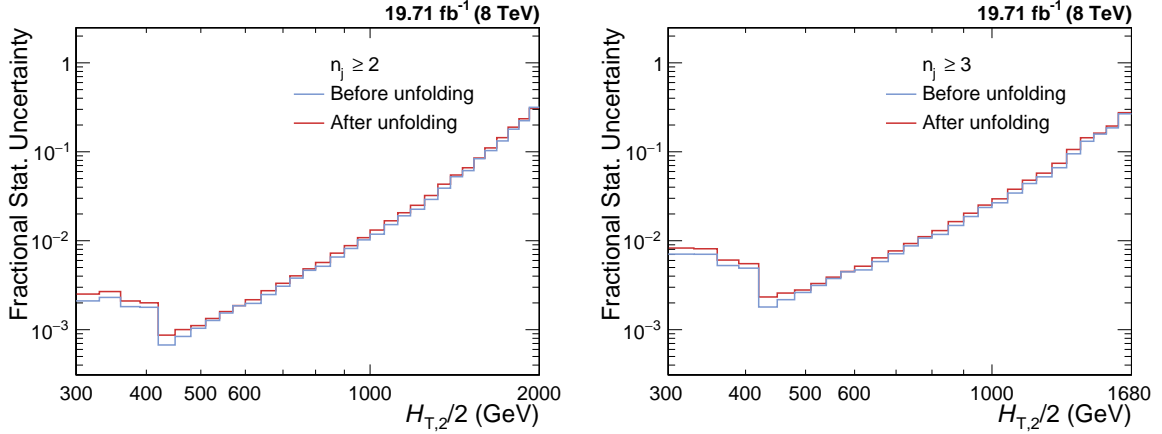


Figure 1.17: The fractional statistical uncertainties of the measured (blue line) and the unfolded data (red line) for inclusive 2-jet events (left) and for inclusive 3-jet events (right). The statistical uncertainty increases slightly after unfolding.

The unfolding procedure also introduces a correlation between bins due to event migrations. There is a significant correlation (anti-) between for neighbouring bins in  $H_{T,2}/2$  whereas the correlation can be negligible between bins which are far off in the phase space. Figure 1.18 shows the correlations of the statistical uncertainty after the unfolding for  $n_j \geq 2$  (left) and  $n_j \geq 3$  events (right). These correlations are must be taken into account while performing the fits to extract the value of the strong coupling constant,  $\alpha_S$ .

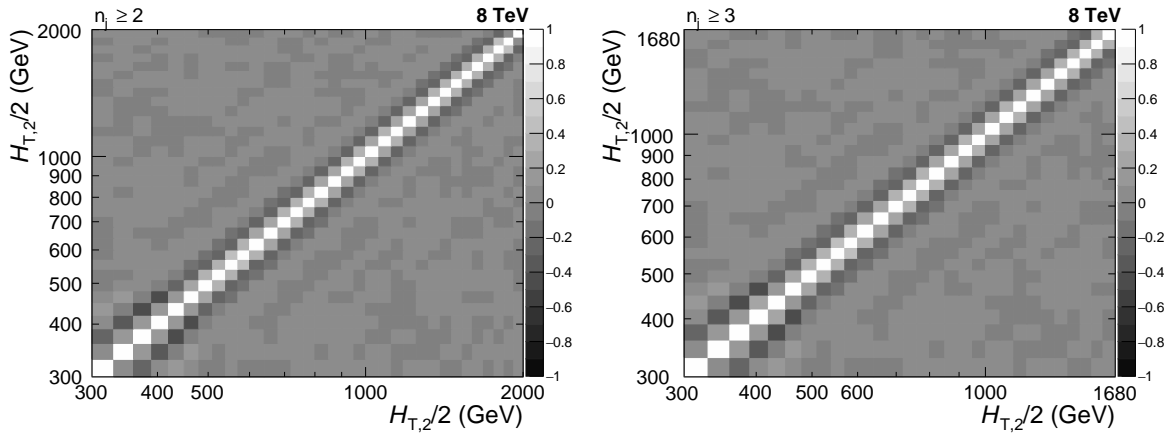


Figure 1.18: Correlations of the statistical uncertainty introduced by the unfolding procedure for inclusive 2-jet events (left) and and 3-jet events (right). There is a significant correlation or anti-correlation between neighbouring bins through bin migrations.

### 1.6.3 Jet Energy Corrections uncertainties

The systematic uncertainty on the measured cross sections is dominated by the jet energy corrections (JEC). These corrections, as explained in Sec. [?](#), correct the measured jet energy for a variety of detector effects. The effect of the JEC has been estimated by varying up and down the energy of all jets by the uncertainty. The observables obtained with these variations are then compared to the nominal distributions in which the observable is obtained with the nominal values of the jet energy. The differences between the nominal distributions and the ones obtained by varying the jet energy scale reflect the effect of the jet energy corrections. There are 25 mutually independent sources which contribute to JEC uncertainty. Each source is fully correlated in  $p_T$  and  $\eta$  but uncorrelated to all other sources and presents a  $1\sigma$  shift. The JEC uncertainties can be asymmetric in nature and hence the upwards and downwards variation of each source are treated separately. The sum in quadrature of all sources gives the total JEC uncertainty. Depending on the origin of sources, they are categorized into four groups which are described below in brief. The details of the jet energy corrections and uncertainties can be found in [\[13\]](#).

The 25 individual uncertainty sources are the following : AbsoluteStat, AbsoluteScale, AbsoluteFlavMap, AbsoluteMPFBias, Fragmentation, SinglePionECAL, SinglePionHCAL, FlavorQCD, RelativeJEREC1, RelativeJEREC2, RelativeJERHF, RelativePtBB, RelativePtEC1, RelativePtEC2, RelativePtHF, RelativeFSR, RelativeStatFSR, RelativeStatEC2, RelativeStatHF, PileUpDataMC, PileUpPtRef, PileUpPtBB, PileUpPtEC1, PileUpPtEC2 and PileUpPtHF.

The AbsoluteFlavMap uncertainty is exactly zero for the 8 TeV and can be ignored. In this way practically 24 uncertainties are considered to calculate JEC uncertainty. For the four sources : RelativeJERHF, RelativePtHF, RelativeStatHF, PileUpPtHF, the JEC uncertainty is exactly zero because of  $|y| < 2.5$  cut used in the analysis. So only 20 sources contribute to the total JEC uncertainty. The



Figures A.1-A.3 show the JEC uncertainty from each source separately for inclusive 2-jet (left) and 3-jet events (middle), respectively. The bin-wise values (in %) are tabulated in the

### 1.6.4 Unfolding uncertainty

The unfolding uncertainty is comprised of three uncertainties :

1. **JER uncertainty** : The jet energy resolution, which was derived in Section 1.4, is used to produce the response matrix using a forward smearing technique in the unfolding procedure. Therefore, a dependence on the jet energy resolution on the unfolded cross section is introduced and a further uncertainty source due to the uncertainty on the jet energy resolution is introduced. Table 1.5 shows the scaling factors, which were applied on reconstructed simulated events to obtain the actual resolution in data. The official recommendations include offset variations of these scaling factors to estimate the uncertainty on the resolution and are also given in Table 1.5. The determination of the resolution is repeated with the upwards and downwards variation of the resolution scaling factor applied. The unfolding procedure is also reiterated using the variations of the resolution and the differences of the obtained cross section to the nominal cross section are accounted for as a systematic uncertainty.
2. **Model dependence** : As explained earlier that to construct the response matrix by Toy MC method, the fitting of the theoretical predictions is performed by using function given in Equation 1.9. To use alternative function for this fitting gives the model dependence of the theoretical  $H_{T,2}/2$  spectrum which affects the response matrix and thus the unfolding. The NLO  $H_{T,2}/2$  spectrum is fitted by the another function described by Equation 1.12. The procedure mentioned in Section 1.5 is repeated to get the new unfolded cross

sections. The differences in unfolded cross sections using the functions given by equations 1.9 and 1.12 gives the unfolding uncertainty.

3. **Additional uncertainty** : As explained in Section 1.4, an additional uncertainty is added from the difference in unfolding on comparing with reduced JER.

All the three uncertainties are added in quadrature to account the unfolding uncertainty which is 1-2% on cross-sections.

### 1.6.5 Total experimental uncertainty

After calculating the uncertainties from all different sources, total experimental uncertainty is obtained by adding in quadrature the uncertainties from individual sources. The bin-wise values (in %) of uncertainties from each source as well as total uncertainty are experimental uncertainty as well as the total uncertainty for inclusive 2-jet (left) and inclusive 3-jet (right) events. The systematic uncertainty on the measured cross sections is asymmetric and dominated by the uncertainty on the jet-energy scale at lower  $H_{T,2}/2$  values and by statistical uncertainty at higher  $H_{T,2}/2$  values. The experimental uncertainties from each source as well as total uncertainty are quoted in Table 1.7.

Table 1.7: Overview of all experimental uncertainties affecting the cross section measurement.

Uncertainty Source	Inclusive 2-jet	Inclusive 3-jet
<b>Statistical</b>	< 1 to 30%	< 1 to 40%
<b>JEC</b>	3 to 10%	4 to 12%
<b>Unfolding</b>	1-2%	1-2%
<b>Luminosity</b>	2.6%	2.6%
<b>Residual uncorrelated</b>	1%	1%

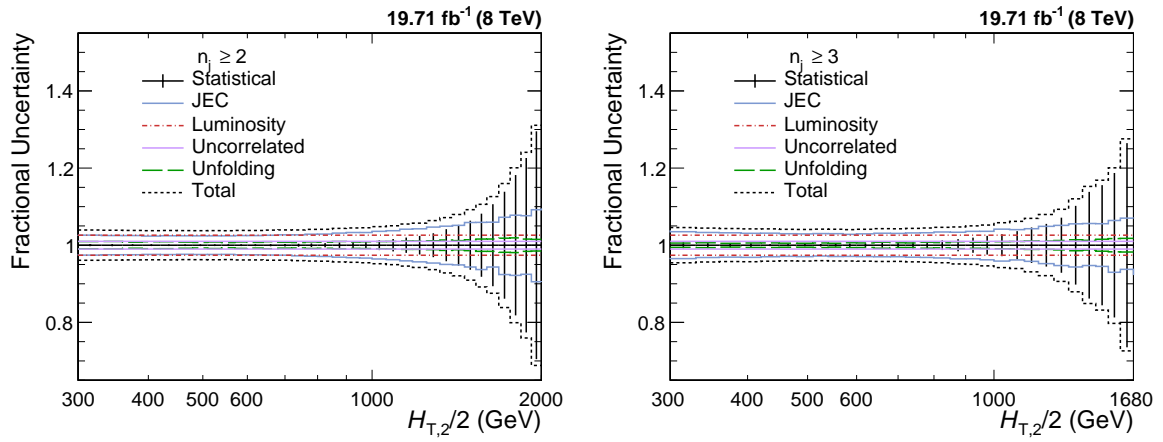


Figure 1.19: Overview of all experimental uncertainties affecting the cross section measurement for inclusive 2-jet (left) and inclusive 3-jet (right). The error bars indicate the statistical uncertainty after unfolding. The colored lines give the uncertainties resulting of jet energy scale, luminosity, unfolding and residual effects. The total uncertainty is calculated by adding in quadrature the individual sources of uncertainty. **JEC** **Unfolding** **Luminosity** **Residual** **uncorrelated**



# Appendix A

## A.1 Individual sources of Jet Energy Correction uncertainties

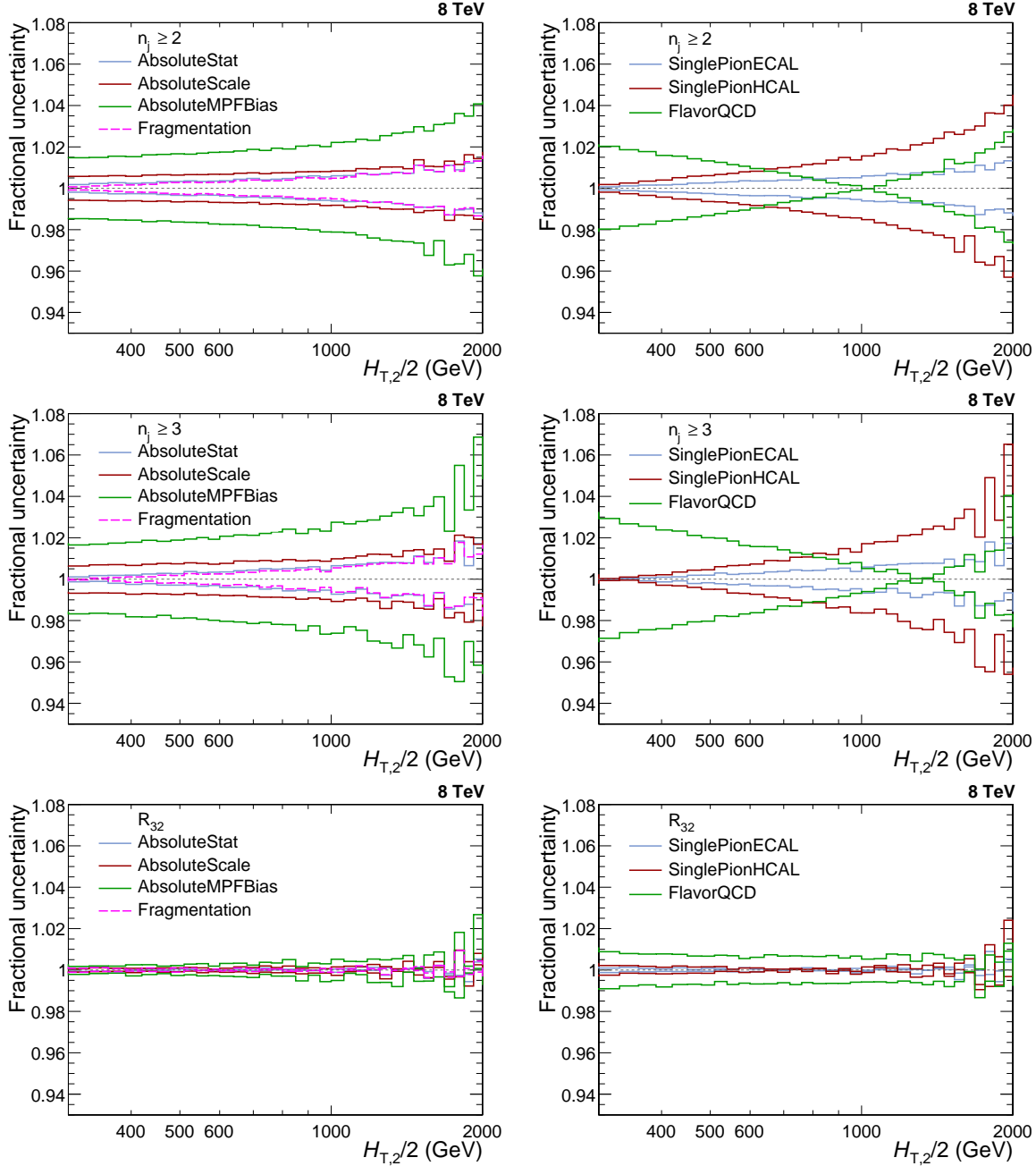


Figure A.1: The relative size of the jet energy correction (JEC) uncertainties for individual sources are shown for inclusive 2-jet (top) and 3-jet events cross sections (middle) and cross section ratio  $R_{32}$  (bottom). On left, JEC uncertainties are evaluated from **AbsoluteStat**, **AbsoluteScale**, **AbsoluteMPFBias** and **Fragmentation** sources whereas on right, these are evaluated from **SinglePionECAL**, **SinglePionHCAL** and **FlavorQCD** sources.

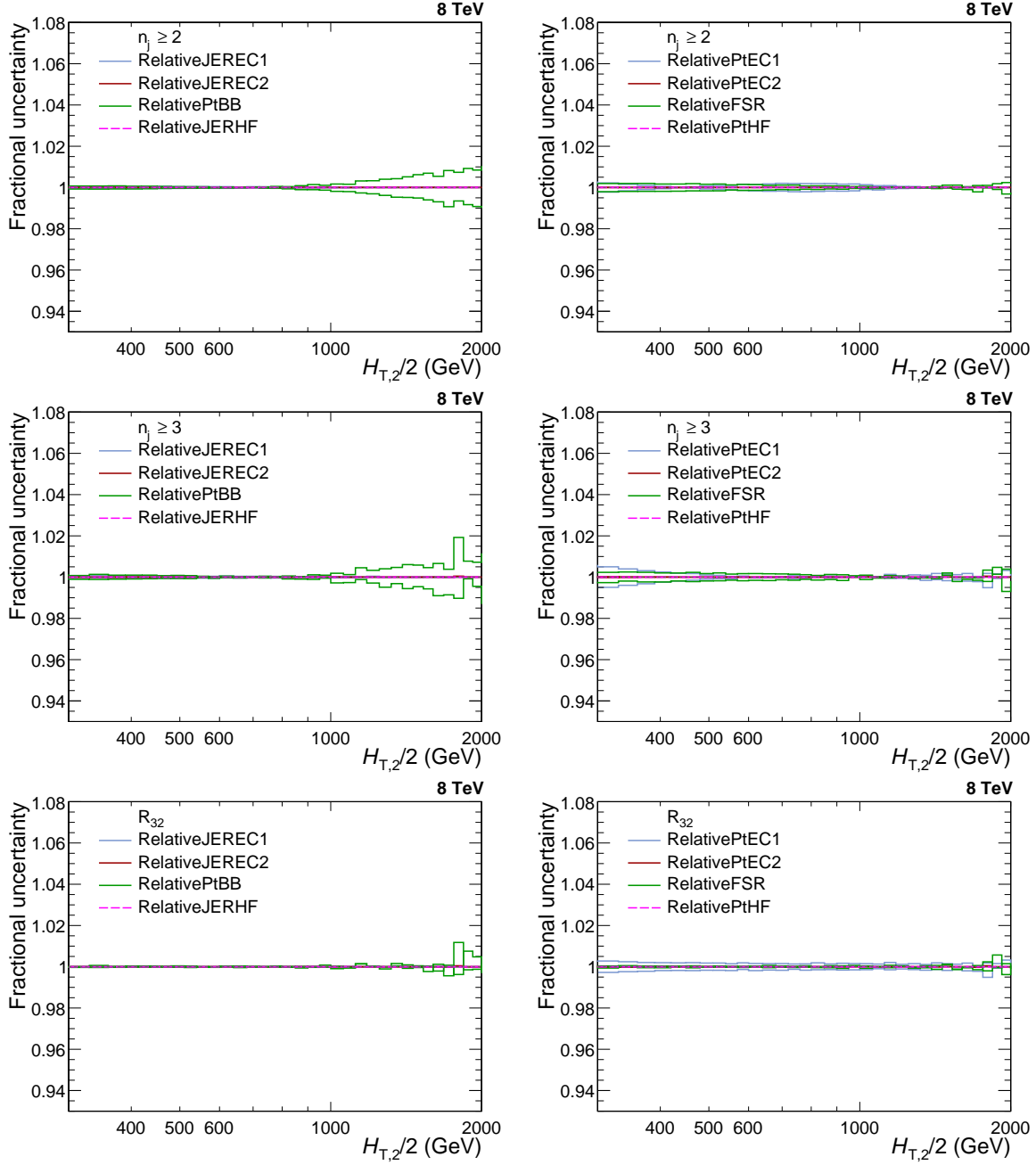


Figure A.2: The relative size of the jet energy correction (JEC) uncertainties for individual sources are shown for inclusive 2-jet (top) and 3-jet events cross sections (middle) and cross section ratio  $R_{32}$  (bottom). On left, JEC uncertainties are evaluated from [RelativeJEREC1](#), [RelativeJEREC2](#), [RelativePtBB](#) and [RelativeJERHF](#) sources whereas on right, these are evaluated from [RelativePtEC1](#), [RelativePtEC2](#), [RelativeFSR](#) and [RelativePtHF](#) sources.

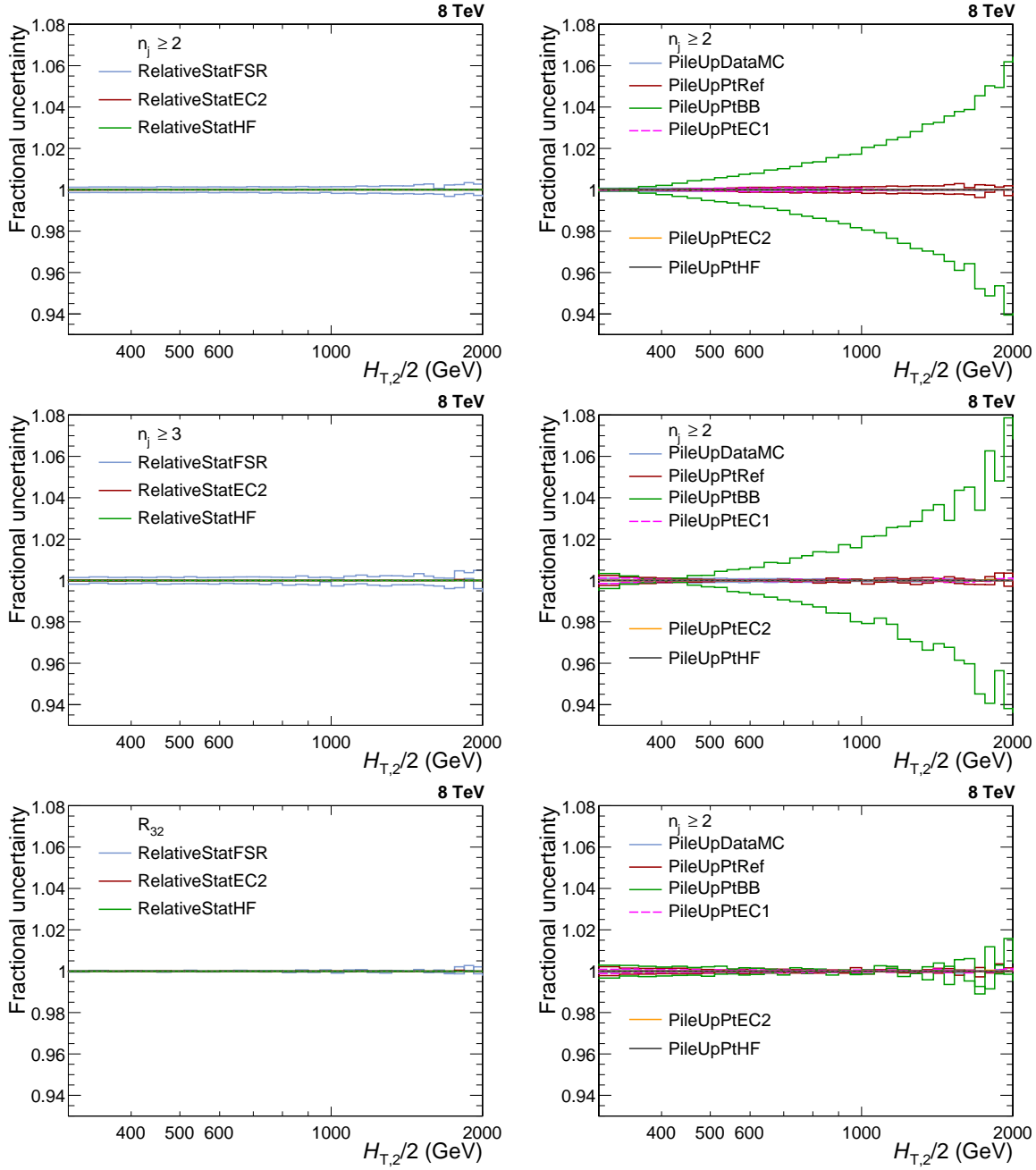


Figure A.3: The relative size of the jet energy correction (JEC) uncertainties for individual sources are shown for inclusive 2-jet (top) and 3-jet events cross sections (middle) and cross section ratio  $R_{32}$  (bottom). On left, JEC uncertainties are evaluated from **RelativeStatFSR**, **RelativeStatEC2** and **RelativeStatHF** sources whereas on right, these are evaluated from **PileUpDataMC**, **PileUpPtRef**, **PileUpPtBB**, **PileUpPtEC1**, **PileUpPtEC2** and **PileUpPtHF** sources.



# Bibliography

- [1] C. J. Clopper and E. S. Pearson, “The Use of Confidence or Fiducial Limits Illustrated in the Case of the Binomial”, *Biometrika* **26**, 404 (1934) doi: [10.2307/2331986](https://doi.org/10.2307/2331986)
- [2] CMS Collaboration, “Jet Identification at 8 TeV”, (2012) URL: <https://twiki.cern.ch/twiki/bin/viewauth/CMS/JetID> (accessed on 2017-10-31).
- [3] CMS Collaboration, “Jet Energy Resolution at 8 TeV”, (2012) URL: <https://twiki.cern.ch/twiki/bin/viewauth/CMS/JetResolution> (accessed on 2016-01-22).
- [4] Johan Alwall *et al.*, “MadGraph 5 : Going Beyond”, *JHEP* **1106**, 128 (2011) doi: [10.1007/JHEP06\(2011\)128](https://doi.org/10.1007/JHEP06(2011)128) arXiv:[1106.0522](https://arxiv.org/abs/1106.0522) [hep-ph].
- [5] Torbjörn Sjöstrand, Stephen Mrenna and Peter Skands, “PYTHIA 6.4 Physics and Manual”, *JHEP* **0605**, 026 (2006) doi: [10.1088/1126-6708/2006/05/026](https://doi.org/10.1088/1126-6708/2006/05/026) arXiv:[hep-ph/0603175](https://arxiv.org/abs/hep-ph/0603175).
- [6] John Alwall *et al.*, “A Standard format for Les Houches event files”, *Comput. Phys. Commun.* **176**, 300 (2007) doi: [10.1016/j.cpc.2006.11.010](https://doi.org/10.1016/j.cpc.2006.11.010) arXiv:[hep-ph/0609017](https://arxiv.org/abs/hep-ph/0609017).

- 
- [7] CMS Collaboration, “Jet Performance in pp Collisions at 7 TeV”, CMS Physics Analysis Summary **CMS-PAS-JME-10-003** (2010) <http://cds.cern.ch/record/1279362>
- [8] CMS Collaboration, “Jet Energy Resolution in CMS at  $\sqrt{s}=7$  TeV” CMS Physics Analysis Summary **CMS-PAS-JME-10-014** (2011) <http://cds.cern.ch/record/1339945>
- [9] G. D’Agostini, “A Multidimensional unfolding method based on Bayes’ theorem”, Nucl. Instrum. Meth. A **362**, 487 (1995) doi: [10.1016/0168-9002\(95\)00274-X](https://doi.org/10.1016/0168-9002(95)00274-X).
- [10] Tim Adye, “Unfolding algorithms and tests using RooUnfold”, Proceedings of the PHYSTAT 2011 Workshop, CERN, Geneva, Switzerland 313 (January 2011) doi: [10.5170/CERN-2011-006.313](https://doi.org/10.5170/CERN-2011-006.313) arXiv:[arXiv:1105.1160](https://arxiv.org/abs/1105.1160) [[physics.data-an](#)].
- [11] CMS Collaboration, “Measurement of the Inclusive Jet Cross Section in  $pp$  Collisions at  $\sqrt{s} = 7$  TeV”, Phys. Rev. Lett. **107**, 132001 (2011) doi: [10.1103/PhysRevLett.107.132001](https://doi.org/10.1103/PhysRevLett.107.132001) arXiv:[1106.0208](https://arxiv.org/abs/1106.0208) [[hep-ex](#)].
- [12] CMS Collaboration, “CMS Luminosity Based on Pixel Cluster Counting - Summer 2013 Update”, CMS Physics Analysis Summary **CMS-PAS-LUM-13-001** (2013) <http://cds.cern.ch/record/1598864>
- [13] CMS Collaboration, “Jet energy scale and resolution in the CMS experiment in pp collisions at 8 TeV,” JINST **12**, P02014 (2017) doi: [10.1088/1748-0221/12/02/P02014](https://doi.org/10.1088/1748-0221/12/02/P02014) arXiv:[1607.03663](https://arxiv.org/abs/1607.03663) [[hep-ex](#)].

*Selected  
Reprints*

